



1 **Fully Coupled High-Resolution Atmosphere-Ocean-Wave**
2 **Simulations of Hurricane Henri (2021): Implications for Offshore**
3 **Load Assessments**

4 Chunyong Jung¹, Pengfei Xue^{1,2,3}, Chenfu Huang^{2,3}, William Pringle¹, Mrinal Biswas⁴, Geeta Nain^{1,2}, and
5 Jiali Wang¹

6 ¹Environmental Science Division, Argonne National Laboratory, Lemont, IL 60439, USA

7 ²Department of Civil and Environmental Engineering, Michigan Technological University, Houghton, MI 49931, USA

8 ³Great Lakes Research Center, Michigan Technological University, Houghton, MI 49931, USA

9 ⁴National Center for Atmospheric Research, Boulder, CO 80310, USA

10 *Correspondence to:* Chunyong Jung (cjung2@anl.gov); Pengfei Xue (pexue@mtu.edu)

11

12 **Abstract.** This study presents a fully coupled modelling system that integrates atmospheric, ocean, and wave models to
13 simulate interactions during tropical cyclones and assess their implications for offshore infrastructure. The system is evaluated
14 using Hurricane Henri (2021), chosen for its distinctive track along the U.S. northeast coast, an area with densely populated
15 regions and offshore wind energy zones. The event is supported by extensive observations, including airborne Doppler radar,
16 dropsondes, sea surface temperature, and ocean surface wave measurements. Three experiments with increasing complexity
17 in atmosphere-ocean-wave coupled processes are conducted to examine their impact on storm intensity and development.
18 Compared to atmospheric-only and atmosphere-ocean coupled simulations, the fully coupled model reduces intensity
19 overestimations and improves the wind structure from near the surface to the upper troposphere. These improvements are due
20 to realistic representation of complex feedback loops between the atmosphere, ocean, and waves. Wave-induced cooling of
21 sea surface temperatures and reduced surface enthalpy flux mitigate intensity overestimation. Additionally, wave-driven
22 surface roughness, reflected in realistic surface roughness length and drag coefficients, enhances the radial and vertical profiles
23 of hurricane boundary layer winds. The fully coupled simulation shows promising potential for assessing risks to offshore
24 infrastructure, featuring a more stable atmospheric boundary layer, weaker surface roughness, and lower turbulent kinetic
25 energy. These factors allow wind veer to persist and align more closely with observations. The system also captures wind-
26 wave misalignment, emphasizing the importance of incorporating ocean and wave components for accurate risk assessments
27 in offshore infrastructure, such as wind turbine operations.

28



29 **1 Introduction**

30 Tropical cyclones (TCs) pose a serious threat to society, bringing destructive winds, large waves, storm surges, heavy rainfall,
31 and compound flooding. Over the past four decades (1980-2019), TCs have led U.S. disaster records, causing the highest
32 economic losses (\$945.9 billion) and fatalities (6,502) among all natural hazards (Smith, 2020). Climate warming further
33 complicates TC behaviour, adding uncertainties: while TC frequency may remain stable or decline, TC intensity is likely to
34 increase in many coastal areas, exacerbating coastal hazards and offshore energy harvesting (Knutson et al., 2010, 2019, 2020;
35 Walsh et al., 2015, 2016; Wang et al., 2024a,b). Consequently, accurate TC prediction has become increasingly essential for
36 effective risk analysis, disaster prevention, and infrastructure design.

37
38 Forecasting TC tracks has improved substantially over the past few decades, while predicting TC intensity remains challenging
39 and has shown only limited progress (DeMaria et al., 2014; Rappaport et al., 2009; Yamaguchi et al., 2017; Zao et al., 2022).
40 Previous studies suggested that insufficient consideration of the physical processes and their subsequent heat and momentum
41 exchanges at the atmosphere-ocean interface might be responsible for the slower progress in improving TC intensity forecasts
42 compared to track forecasts over the decades (DeMaria et al., 2007; Zhao et al., 2017, 2022). For example, Mogensen et al.
43 (2017) and Wei et al. (2017) suggest that sea surface temperature (SST) cooling feedback process in TC modelling is a major
44 factor contributing to bias in TC intensity forecasts. The storm extracts energy from the ocean through exchanges of heat,
45 moisture, and momentum fluxes at the atmosphere and ocean interface. TC-driven high winds and waves enhance turbulent
46 mixing in the upper ocean, resulting in SST cooling—often called "cold wakes"—along the storm's path. This process acts as
47 negative feedback on storm energetics by reducing the surface enthalpy flux supply (Bender et al., 1993; Cavaleri et al., 2012;
48 Cione and Uhlhorn, 2003; Fan et al., 2010; Schade and Emanuel, 1999). For instance, Zhu and Zhang (2006) found that cooling
49 in SST, averaging -1.3 °C near the TC centre and along its track, statistically weakens hurricane intensity by about 25 hPa.
50 This feedback mechanism between the atmosphere and ocean is primarily driven by vertical mixing of cooler waters from
51 beneath the seasonal thermocline, induced by TC-generated strong waves, large upper-ocean shears, and upwelling from
52 divergent ocean currents (Emanuel, 1986; Schade and Emanuel, 1999; Wu et al., 2016). The reduced surface heat exchange
53 then weakens the moist enthalpy flux from the ocean to the atmosphere, thereby diminishing TC intensity. Therefore, to
54 realistically capture TC-induced SST cooling, the atmospheric forecast model must be coupled with a three-dimensional ocean
55 model (e.g., Yablonsky and Ginis, 2009).

56
57 Another key ocean element in TC evolution involves ocean surface waves, which significantly affect both atmospheric and
58 ocean dynamics. As for the impact of the waves on atmospheric dynamics, on the one hand, ocean surface waves characterize
59 surface roughness, influencing the structure of atmospheric and marine boundary layers. This, in turn, affects atmosphere-
60 ocean momentum and heat exchanges, upper-ocean mixing, sea spray production, and albedo (Cavaleri et al., 2012). Liu et al.
61 (2011) found that their satellite-based latent heat flux data (XseaFlux) performed significantly better in capturing TC-



62 associated latent heat flux by incorporating sea surface wave features such as wave breaking, wave orbital motion (non-
63 breaking waves), and sea spray. Chen et al. (2007, 2013) emphasized the importance of wind-wave feedback under extreme
64 conditions through directional wind-wave coupling, which enhances simulations of hurricane-induced surface winds and
65 hurricane structure. Similarly, Zhao et al. (2017, 2022) found that wave-induced processes, including mixing and sea spray
66 production, reduce biases in TC intensity forecasts, underscoring the essential role of ocean surface waves in atmosphere-
67 ocean enthalpy flux exchanges and TC evolution. On the other hand, breaking waves also generate sea spray, which enhances
68 atmosphere-ocean heat and moisture flux exchanges under tropical cyclone (TC) conditions, potentially intensifying TCs
69 (Perrie et al., 2004, 2005; Richter and Stern, 2014; Zhao et al., 2022). However, Prakash et al. (2019) found that incorporating
70 sea spray has only a marginal effect on storm intensity, suggesting that wave impacts on surface roughness may play a more
71 significant role in the coupling process. This relative importance, however, requires further investigation with additional storm
72 cases, as will be discussed in Section 6.

73
74 As for the impact of the waves on ocean dynamics, wave-induced mixing—driven by both breaking and non-breaking waves
75 plays a key role in modulating SST, which is critical for TC development and intensity (Babanin, 2006; Qiao et al., 2004;
76 Sullivan and McWilliams, 2010). Breaking waves create surface-level turbulence, but kinetic energy dissipates quickly with
77 depth, limiting their influence on SST and surface heat fluxes (Craig and Banner, 1994; Zhang et al., 2007). In contrast, non-
78 breaking waves penetrate deeper, significantly affecting SST and mixed layer depth, both of which are essential for TC
79 intensity modification (Babanin et al., 2009; Qiao et al., 2004; Zhang et al., 2022). Additionally, waves influence the bottom
80 boundary condition for TCs through wave-current interactions, affecting sea surface currents (Lane et al., 2007; Mellor, 2016;
81 Olabarrieta et al., 2010; Smith, 2006) and SST through mechanisms such as radiation stress, Stokes drift, and vertical mixing
82 (Wang et al., 2024b). Coupled wind-wave-ocean models underscore the significant impact of wind-wave-current interactions
83 on atmosphere-ocean momentum flux and ocean responses in TCs (Fan et al., 2009).

84
85 Grid spacing is another critical factor being continually addressed as computational resources increase over time. Resolving
86 the inner core of a TC with a grid spacing of 4 km or less has enabled the explicit representation of deep convection, leading
87 to a more accurate depiction of TC structure in the atmospheric component (e.g., Gentry and Lackmann, 2010). In an
88 atmosphere-ocean coupling framework, Tsartsali et al. (2022) emphasized that optimal results require higher resolutions in
89 both ocean and atmospheric models, specifically at least eddy-permitting (~25 km) and better eddy-resolving (~8 km) ocean
90 resolution, along with comparable atmospheric resolution, for reliable atmosphere-ocean coupling along the Gulf Stream.
91 Additionally, Zhang et al. (2023) employed the Community Earth System Model at very high spatial resolutions (up to 3 km
92 for the ocean and 5 km for the atmosphere) to capture major weather and climate extremes, highlighting the importance of
93 convection-permitting resolution and sub-mesoscale ocean eddies in modelling TC dynamics and eddy-mean flow interactions.

94

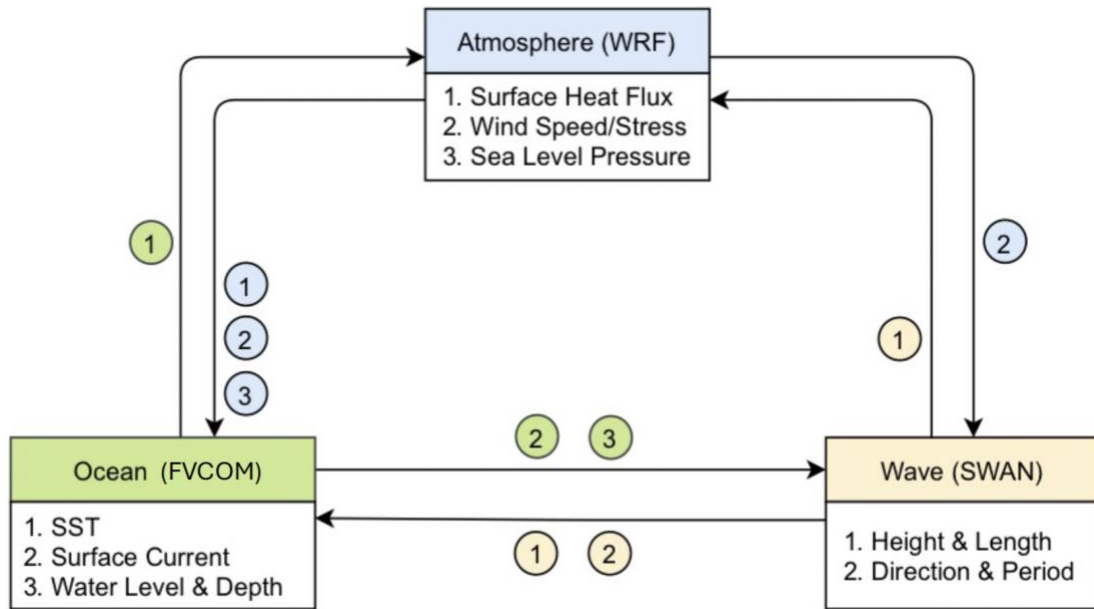


95 This study introduces a newly developed atmosphere-ocean-wave coupled modelling system that integrates a regional
96 atmospheric climate model with ocean and surface wave models, both of which operate on a high-resolution unstructured
97 mesh. This framework, while sharing similarities with the Coupled Ocean Atmosphere Wave and Sediment Transport
98 (COAWST, Warner et al., 2010) model in its coupled components, distinguishes itself through its ability to provide regional
99 refinement over areas of interest (e.g., offshore wind farms). Its capability to generate ultra-high spatial resolution for the ocean
100 mesh allows for more detailed and localized information, enhancing its applicability for site-specific analyses. In addition, we
101 incorporate the impacts of non-breaking waves into the coupling system to enable more realistic interactions between the
102 atmosphere, ocean, and waves. Utilizing this fully coupled system at a very high resolution (3 km for the atmosphere and 3
103 km for the ocean and wave models near the U.S. Northeast Coast), we investigate the effects of atmosphere-ocean-wave three-
104 way feedback on tropical cyclone (TC) development and demonstrate its relevance in assessing potential TC-induced risks for
105 offshore wind infrastructure. The model presented here provides a more realistic depiction of the complex interactions between
106 the ocean, waves, and atmosphere compared to many existing statistical-parametric models (e.g., Arthur, 2021; Chen et al.,
107 2024; Roldán et al., 2023) and idealized TC models (e.g., Sanchez Gomez et al., 2023), which often analyse wind and wave
108 interactions separately or exclude them altogether. These limitations may result in incomplete risk assessments, as wave
109 dynamics play a substantial role in TC behaviour and evolution, as previously discussed.

110

111 The development of the model, including detailed information on each model component and the coupler, is described in
112 Section 2. Section 3 describes the experimental design and data used for model validation using Hurricane Henri (2021) as a
113 working example. In Section 4, we present results and analysis. Implications for potential risks to offshore wind energy is
114 discussed in Section 5, followed by the summary and discussions in Section 6.

115



116

117 **Figure 1. Schematic of coupled atmosphere-ocean-wave system and modelling used in this study.**

118

119 **2 Model Description**

120 The coupled atmosphere-ocean-wave modelling system consists of three components: the Weather Research and Forecasting
121 (WRF) model for atmospheric processes (WRF V4.5.1; Skamarock et al., 2019), the Finite Volume Community Ocean Model
122 (FVCOM V4.3.1; Chen et al., 2003, 2013) for ocean circulations, the third-generation Simulating WAVes Nearshore (SWAN)
123 model for wave dynamics (Booij et al., 1999), and a coupler to exchange data fields (Fig. 1). Hereinafter, we refer to the
124 coupled WRF-FVCOM-SWAN model as C-WFS. In the three-way coupled framework of C-WFS, the model components are
125 executed in parallel, exchanging information through the Ocean Atmosphere Sea Ice Soil3 (OASIS3)-Model Coupling Toolkit
126 (MCT) coupler (Craig et al., 2017). We describe each component, improvements made to them, and the approach to coupling
127 in Sections 2.1-2.2.

128 **2.1 Model Components**

129 WRF is a nonhydrostatic, quasi-compressible atmospheric model with boundary layer physics schemes and a variety of
130 physical parameterizations of sub-grid scale processes for predicting meso- and macroscales of motion. WRF has been
131 extensively used for operational forecasts as well as for realistic and idealized research experiments. We have modified the
132 WRF code to enable the wave slope-based sea surface roughness formulation from Taylor and Yelland (2001) in several



133 surface schemes (MYNN[Nakanishi and Niino, 2009; Olson et al., 2019], and the original and revised MM5 [Dyer and Hicks,
134 1970; Jimenez et al., 2012; Paulson, 1970; Webb, 1970]):

$$135 \quad Z_0 = 1200H_s \left(\frac{H_s}{L_p} \right)^{4.5} + \frac{0.11\nu}{u_*} \quad Z_0 \leq 0.00285 \quad (1)$$

136
137 where Z_0 is the surface roughness length, H_s is the significant wave height, L_p is the wavelength at the peak of spectrum, ν is
138 kinematic viscosity, and u_* is the friction velocity. Other wave-based formulations (e.g., Drennan et al., 2003) are also available
139 in C-WFS but in our testing we found that the capped Taylor and Yelland (2001) method gave the best performance for our
140 case study.

141 The ocean model component, FVCOM, is a prognostic, free-surface, 3-D primitive equation coastal ocean circulation model
142 that is numerically solved over an unstructured triangular grid using the finite-volume method. Version 4.3.1 of FVCOM is
143 used in this study, allowing ocean hydrodynamic conditions to interact freely with atmospheric conditions throughout the
144 simulation period. We modified the FVCOM code to incorporate vertical mixing effects induced by non-breaking waves. Non-
145 breaking wave induced mixing is added to the turbulence eddy diffusivity B_v included in the ocean model and is expressed as
146 (Ghantous and Babanin, 2014a,b; Aijaz et al. 2017):

$$147 \quad B_v = \alpha A^3 \kappa \sigma e^{3\kappa z} \quad (2)$$

148
149 where $\alpha = 0.1$, A = wave amplitude ($H_s/2$), κ = wave number ($2\pi/L$), σ = peak wave frequency ($1/T_p$), z is water depth.
150 The wave model component, SWAN v41.01, is a third-generation spectral wave model developed at Delft University of
151 Technology that computes random, short-crested wind-generated waves in coastal regions and inland waters
152 (<http://swanmodel.sourceforge.net/>). It solves the evolution equation of wave action density in space time, frequency and wave
153 direction dimensions (Pringle and Kotamarthi, 2021). Various wave energy sources and sinks are modelled, including wave
154 generation by wind, wave decay due to whitecapping, bottom friction, depth-induced wave breaking, and energy redistribution
155 through nonlinear wind-wave interactions.
156

157 **2.2 Coupler and Coupling**

158 OASIS3-MCT is a parallelized coupler that enables the simultaneous coupling of 2-D and 3-D fields. Figure 1 provides a
159 schematic illustration of the C-WFS, detailing the quantities exchanged within the coupling framework. The friction velocity,
160 surface winds, sea level pressure, latent and sensible heat fluxes, and shortwave and longwave radiation fluxes predicted by
161 WRF are transferred to FVCOM as surface forcing, while FVCOM provides sea surface temperature (SST) to WRF as over-
162 ocean boundary conditions. WRF supplies wind fields to drive SWAN for wave simulation, while SWAN provides significant
163 wave height and wavelength at the peak of the spectrum to WRF, which uses them to calculate sea surface roughness based
164 on equation (1). The wave fields are used by FVCOM to compute radiation stress gradients, enabling wave-driven flows,



165 Stokes velocities for mass flux transport, wave-enhanced bottom stresses, and non-breaking wave-induced mixing. Breaking
166 wave induced mixing is incorporated as a part of radiation stress gradients. Additionally, FVCOM provides sea surface currents
167 to SWAN, allowing for the inclusion of Doppler effects from background currents on surface waves. This integration enables
168 SWAN to better account for how ocean current movement affects wave behaviour, resulting in more accurate wave predictions.

169 **3 Application of C-WFS Modelling System**

170 This section describes the C-WFS setup used to simulate Hurricane Henri (2021). Henri reached Category 1 on the Saffir-
171 Simpson scale and made landfall in Rhode Island, U.S. on 22nd August 2021. Despite its relatively weak intensity, the storm
172 brought very heavy rainfall over the Northeastern U.S., including New England, causing widespread flooding and power
173 outages in the densely populated regions, such as New York and Boston. Moreover, Henri is one of the recent TCs to pass
174 through the offshore leased wind energy area in the U.S. northeast continental shelf. During this hurricane, comprehensive
175 observation datasets were collected, including airborne measurements such as doppler radars and dropsondes that reached the
176 eyewall and core. These conditions and datasets allow for direct comparisons between the modelled and observed TC
177 structures, providing insights into model performance and the coupling effects due to atmosphere-ocean-wave interactions.

178 **3.1 Experimental Design and Configuration**

179 To explore the integrated effects of ocean and ocean surface wave related physical processes on TC simulations, a set of three
180 model simulations is performed. WRF standalone simulation is named as experiment 'A', in which the event is modelled using
181 WRF alone with prescribed SST at 6-hour intervals. In experiment 'AO,' WRF is coupled with FVCOM, enabling variable
182 exchange as shown in Fig. 1, but without considering ocean surface wave-related physical processes. Experiment 'AOW' is a
183 multi-way fully coupled experiment, in which WRF, FVCOM, and SWAN exchange variables with each other every hour
184 through the OASIS3-MCT Coupler to allow direct and indirect atmosphere-ocean-wave interactions, as discussed in Section
185 2.

186 All simulations are initialized at 18:00 UTC on August 19, 2021, within a domain encompassing the western North Atlantic
187 Ocean. The atmospheric domain features a horizontal resolution of 3 km (Fig. 2a). The ocean domain, which covers a
188 substantial portion of the WRF ocean domain, employs an unstructured triangular grid with resolutions ranging from 3 km
189 near the coast to 9 km in the open ocean, effectively resolving the complex coastline of the U.S. Northeast Coast (Fig. 2b).
190 Initial and boundary conditions for the atmosphere model are obtained from the 6-hourly 0.25° NCEP (National Centers for
191 Environmental Prediction) Global Forecast System (GFS; NCEP, 2015) data. Note that the prescribed SST for experiment 'A'
192 is provided by GFS at 6-hourly intervals. The atmosphere is represented by 46 stretched vertical levels topped at 50 hPa with
193 12 layers below 100 metres. The physics selected for this study include the WRF single-moment 6-class microphysics scheme
194 (WSM6; Hong and Lim, 2006), the Rapid Radiative Transfer Model for GCMs longwave and shortwave schemes (Iacono et
195 al., 2008), the Yonsei University PBL (Hong et al., 2006), and the Eta similarity surface layer scheme which is based on the



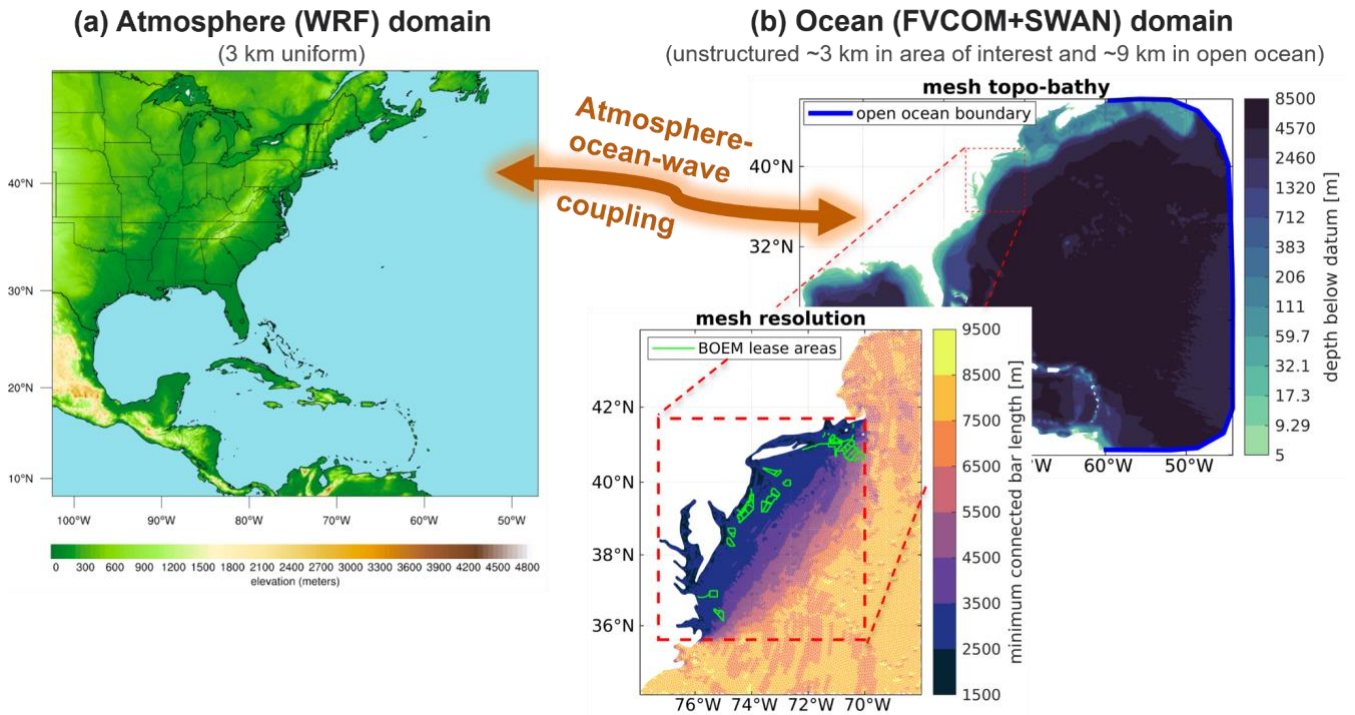
196 revised MM5 Monin-Obukhov scheme (Jimenez et al., 2012). The land surface processes are modelled by the Noah (Chen and
197 Dudhia, 2001). No cumulus parameterizations are used in our WRF setup, as previous studies have demonstrated that a
198 resolution of 4 km or less is adequately convection-permitting in WRF for simulating extreme events (Akinsanola et al., 2024;
199 Kouadio et al., 2020; Qing and Wang, 2021; Sun et al., 2016).

200 Initial conditions for the ocean model fields of currents, water level, salinity, and temperature and boundary conditions for
201 currents, salinity, and temperature are derived from the $(1/12)^\circ \times (1/12)^\circ$ resolution HYbrid Coordinate Ocean Model
202 (HYCOM; Cummings and Smedstad, 2014) analysis data (<http://hycom.org/dataserver/>) simulations. The ocean domain
203 employs varying horizontal resolution of ~9 km in the open ocean down to ~3 km over the continental shelf in the area of
204 interest (Fig. 2b). The ocean is represented vertically with 40 sigma layers, enabling the model to accurately reflect the abrupt
205 changes in coastal bathymetry. Vertical mixing processes are simulated using the Mellor–Yamada level-2.5 (MY25) turbulence
206 closure model (Mellor and Yamada, 1982), and horizontal diffusivity is computed using the Smagorinsky numerical
207 formulation (Smagorinsky, 1963).

208 For this study, the wave model domain covers the same geographic extent as the FVCOM domain with approximately 12 km
209 horizontal resolution. The wave spectrum is discretized into 36 directional bins and 24 frequency bins on the interval [0.04, 1]
210 Hz. We use Komen et al. (1984) wave growth and whitecapping physics, Madsen et al. (1988) bottom friction, and a constant
211 depth-limiting wave breaker index, all with their default parameters. Lateral boundary conditions for swell are not applied due
212 to their insignificance at the eastern boundary.

213 All experiments involved a 102-hour integration, initialized from the same conditions at 18:00 UTC on August 19, 2021.
214 Following initialization, the simulations evolved freely throughout the entire 102-hour hindcast period without any technical
215 interventions. While nudging techniques, such as spectral nudging of variables such as wind, air temperature, and geopotential
216 height, are valuable for improving modelled tracks, they were intentionally not applied in this study. This decision reflects the
217 focus on exploring the impacts of multi-factor coupling between the atmosphere, ocean, and waves on tropical cyclone (TC)
218 characteristics. Applying nudging could complicate efforts to isolate the specific coupling effects of ocean and wave processes
219 on TC behaviour.

220 Several additional simulations were conducted using different planetary boundary layer and microphysics parameterizations,
221 as well as various forcing data (e.g., ERA5 reanalysis data, the fifth generation of ECMWF atmospheric reanalyses of the
222 global climate). The results consistently showed that the overall conclusions of this study remained unchanged, demonstrating
223 the robustness of the findings and their low sensitivity to these configuration choices.



224
225

226 **Figure 2.** (a) WRF model domain with terrain height elevation, and (b) FVCOM and SWAN domain with bathymetric depths and
227 a zoom-in to the refined mesh grid along the northern U.S. East Coast and BOEM offshore lease areas.

228 3.2 Method and Data

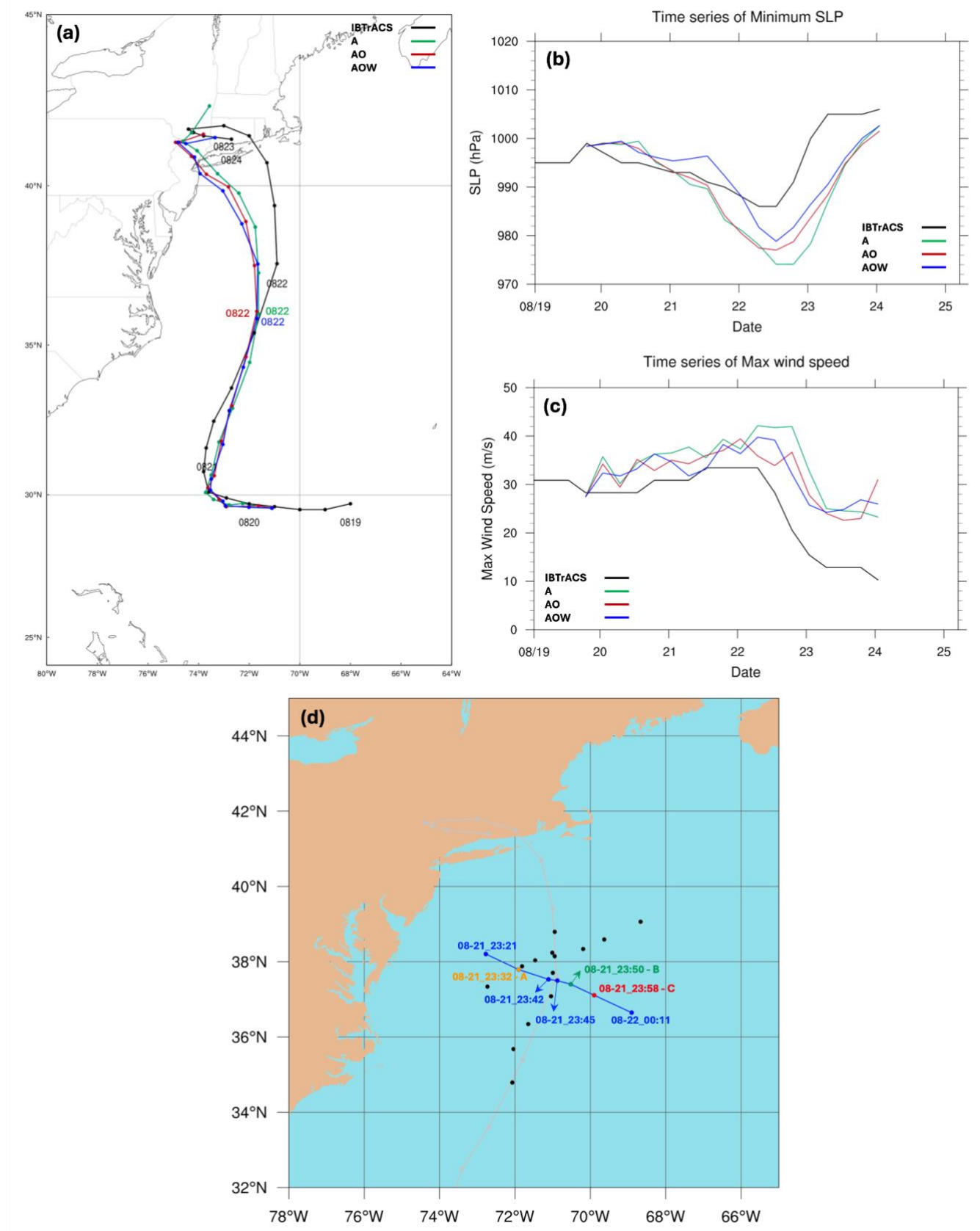
229 The model results are evaluated against observations using multiple datasets, including International Best Track Archive for
230 Climate Stewardship (IBTrACS; Knapp et al., 2010) and airborne observations. IBTrACS is the most complete global
231 collection of TCs, providing TC best position, minimum sea level pressure (SLP), maximum sustained wind speeds, and
232 translation speed at mostly 6-hourly intervals. The airborne observations include the Tropical Cyclone Radar Archive of
233 Doppler Analyses with Recentering (TC-RADAR) dataset (Fischer et al., 2022) and dropsondes from aircraft provided by the
234 National Oceanic Atmospheric Administration’s (NOAA) Hurricane Research Division (HRD). TC-RADAR is a
235 comprehensive database of airborne observations of TCs, featuring data from the X-band tail Doppler radar on NOAA’s WP-
236 3D aircraft. This radar scans in both front and back directions, enabling detailed 3-D analyses of the inner-core structure of
237 TCs. Typically, each mission includes 3-4 passes through the centre of the storm. For each central pass, an analysis is created
238 using a technique called “recentering,” which provides analyses on storm-cantered grids. We utilize storm-centred coordinates
239 for our simulations, aligning the grids of TC-RADAR to enable direct comparison of the 3-D storm structure between the
240 simulations and TC-RADAR. To align with the storm-centred grids of the TC-RADAR analyses, a 300 km × 300 km grid box
241 is centered on the grid cell with the minimum SLP in each dataset. To provide seamless observations from the surface up to



242 0.5 km—the range not covered by TC-RADAR—we use dropsonde data as well. In this study, the model generates tracks and
243 translational speeds that differ slightly from the observations (Fig. 3). Therefore, the positions of the dropsondes are adjusted
244 relative to the storm centre rather than using their actual deployment locations. Here, we selected the seven dropsonde
245 observations shown as blue and colour dots in Fig. 3d for the assessment because they were deployed from a single flight
246 across the storm centre. This flight spanned from the eastern to the western edge within 50 minutes, just 12 hours before the
247 storm reached its peak intensity.

248 Modelled ocean surface waves are compared with observations from two National Data Buoy Center (NDBC; NDBC, 2008)
249 buoys, 41001 and 41002, located on the left of the storm track on the continental slope. While there are more buoy locations,
250 our focus is on the variation of storm-induced winds and waves along Henri’s track. We exclude stations near the U.S Northeast
251 Coast due the models’ track bias after 22nd August (more discussion in Section 4). The buoy data provides surface wind and
252 wave information, including surface wind speed, significant wave height, and peak wave period and direction. In addition to
253 in-situ NDBC buoy measurements, we compiled a series of daily SST data from the Operational Sea Surface Temperature and
254 Ice Analysis (OSTIA; Good et al., 2020) at $0.05^\circ \times 0.05^\circ$ resolution to determine the pre- and post-storm environment as well
255 as the difference between them.

256 The radius of maximum wind (RMW) defines the location of the maximum winds in a TC and is critical to understanding
257 intensity change as well as hazard impacts. In this study, we azimuthally average the vertical profiles of the seven dropsondes
258 and the simulations of wind speed relative to RMW to define the areas within and beyond the eyewall, allowing for a detailed
259 comparison of the storm's inner- and outer-core regions.





261 **Figure 3. Comparison of the simulated (a) track, (b) minimum sea-level pressure (SLP), and (c) maximum surface wind speed of**
262 **Hurricane Henri with the best track during the period from 18 UTC on 19 August to 00 UTC on 24th August 2021. Black lines**
263 **represent values derived from IBTrACS observations. Green lines indicate the experiment ‘A,’ red lines depict the experiment ‘AO,’**
264 **and blue lines show the experiment ‘AOW.’ Figure (d) describes IBTrACS best track (grey line and dots) and dropsonde deployed**
265 **positions (black and colour dots) during Hurricane Henri. Seven dropsondes (blue and colour dots) along the blue line are selected**
266 **to assess model performance.**

267 **4 Model Validation**

268 **4.1 Track and Intensity, and Storm Structure**

269 **4.1.1 Track and Intensity**

270 Figure 3 presents the tracks, SLP minima, and surface wind speed maxima derived from the three simulations alongside
271 IBTrACS. The results indicate that variations in Henri's tracks across the three experiments are minimal (Fig. 3), consistent
272 with previous findings suggesting that TC tracks are predominantly controlled by large-scale atmospheric circulation
273 processes, rather than by atmosphere-ocean interactions at the temporal and spatial scales resolved in these models (e.g.,
274 Zambon et al., 2014). The root-mean square error (RMSE, Table 1) of position indicates all three simulations have similar
275 track errors, with values of 123.7 km for ‘A’, 119.4 km for ‘AO’, and 126.1 km for ‘AOW.’ The relatively high error values
276 are mainly due to significant deviations from the observed track after 00 UTC on 22nd August. These deviations are likely
277 linked to biases in midlatitude upper-level atmospheric wave patterns, such as troughs and ridges, and their interactions with
278 the storm, as the storms are deeply embedded in the baroclinic zone. Preliminary tests show that applying zonal and meridional
279 nudging to winds, geopotential heights, and air temperature above the boundary layer can effectively improve track accuracy.
280 However, as previously discussed, the primary objective of this study is to explore atmosphere-ocean-wave interactions in
281 simulating the evolution and development of Hurricane Henri. Consequently, all results presented in the following sections
282 are derived from simulations conducted without the use of any nudging techniques.

283
284 In terms of minimum SLP for the simulation of Henri's intensity (Fig. 3b), noticeable differences between the modelled storms
285 begin to emerge 12 hours after the simulation starts. While all three simulated storms show an overestimation throughout
286 nearly the entire lifecycle of the storm, especially when they reach their peak at 12 UTC on 22nd August, the magnitude of this
287 overestimation is reduced in ‘AO’ and ‘AOW’ experiments compared to ‘A.’ In ‘AOW’, the overestimation of minimum SLP
288 is delayed until 00 UTC on 22nd August. It then reaches the weakest minimum SLP value, resulting in the lowest RMSE in
289 minimum SLP among the three simulations (Table 1). These temporal trends also apply to the maximum surface wind speed
290 (Fig. 3c and Table 1), demonstrating a reduction in overestimation of maximum surface wind speed in both ‘AO’ and ‘AOW’
291 experiments compared to ‘A.’ Between the experiments ‘AO’ and ‘AOW,’ while ‘AOW’ generally exhibits weaker wind
292 speeds compared to ‘AO,’ it becomes stronger as the storm approaches and reaches its peak intensity, in contrast to the findings
293 for minimum SLP. The potential physical processes underlying this discrepancy are discussed in Section 4.3. It is important
294 to note that the maximum wind speeds recorded in the three simulations represent the peak values at a given time on an hourly



295 basis, which do not fully capture the sustained wind conditions or the broader characteristics of the simulated storms. On the
296 other hand, the observed maximum wind speeds are recorded at a single location and time step, which may not adequately
297 reflect the full extent of potential damage caused by high wind conditions. Therefore, a more thorough evaluation of storm
298 structure, both near the surface and across multiple altitudes, is necessary to provide a more complete assessment of the model's
299 performance.

300
301 **TABLE 1. Root mean square error (RMSE) for each simulation in terms of minimum sea level pressure (hPa),**
302 **maximum surface wind speed (m s^{-1}), and cyclone track (km).**

Experiment	Minimum sea level pressure (hPa)	Maximum surface wind speed (m/s)	Cyclone track (km)
A	9.4	10.2	123.7
AO	7.9	8.7	119.4
AOW	6.4	8.3	126.1

303

304 4.1.2 Storm Structure

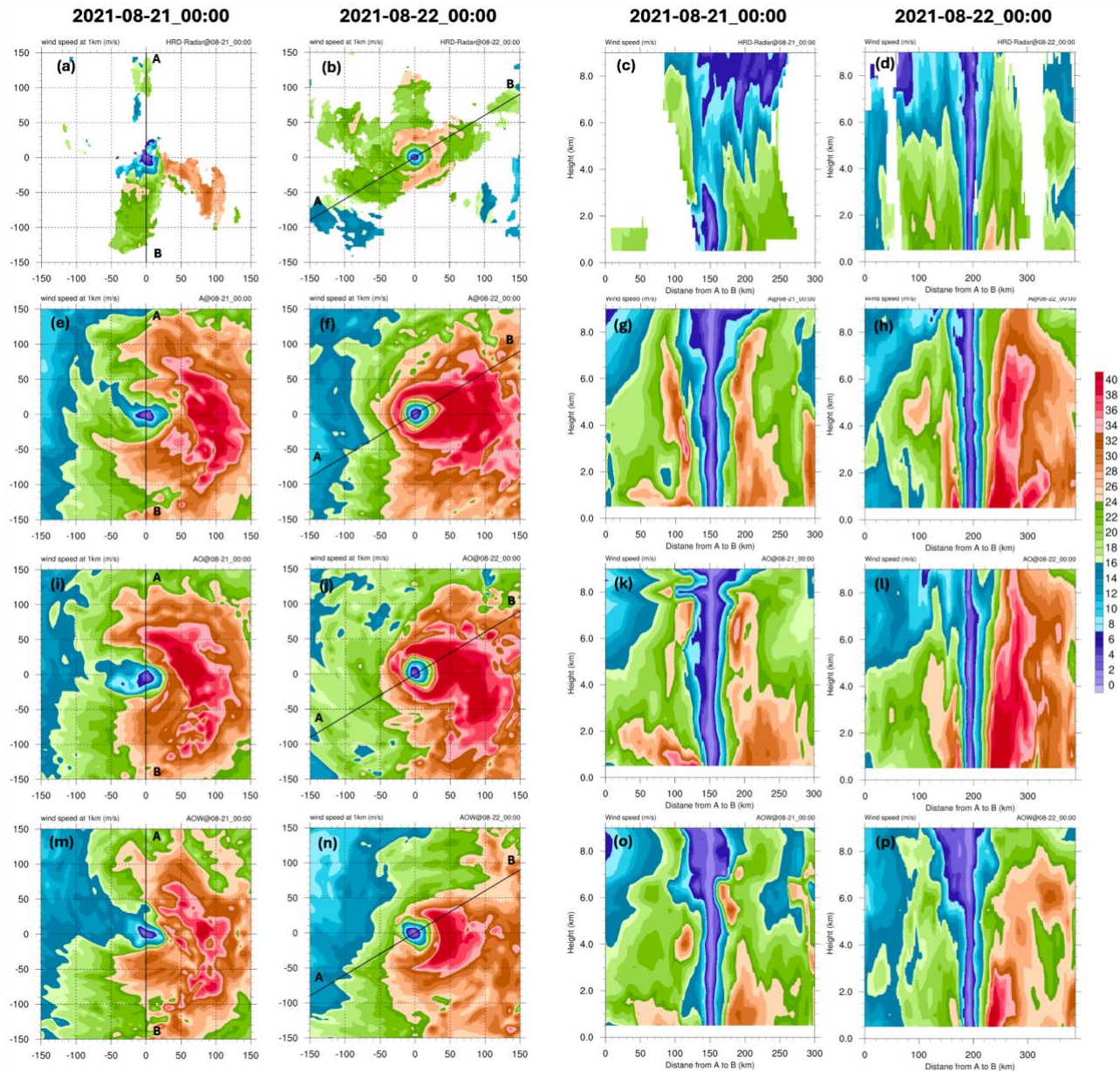
305 Here we examine the model's performance in simulating the three-dimensional storm structure of Henri. Figures 4a-d show
306 the airborne Doppler radar-observed (TC-RADAR) wind speeds at 1-km level and vertical profiles in Henri at 00 UTC on 21st
307 and 22nd August 2021 along the black lines shown in Figs. 4a-b. On 21st August, the storm shows a distinct asymmetric
308 distribution of strong winds, primarily concentrated on the right side—a characteristic of a tropical storm transitioning into a
309 hurricane (Fig. 4a). This asymmetry is largely due to the combination of the storm's poleward movement and its cyclonic
310 circulation. As Henri moves northward during this period, the winds on the right side effectively combine with the storm's
311 forward motion, leading to higher wind speeds. The vertical cross-section of wind speed along the line from A to B, shown in
312 Fig. 4a, offers a different perspective by contrasting the winds between the northern and southern areas. It shows that wind
313 speeds exceeding 20 m s^{-1} are mostly concentrated below 4-km level in the southern part, while strong winds extend up to 8-
314 km level in the northern part at this time (Fig. 4c). At 00 UTC on 22nd August — 12 hours before reaching peak minimum SLP
315 intensity, Henri exhibited a compact and nearly closed distribution of strong winds exceeding 24 m s^{-1} along the eyewall. This
316 demonstrates a more organized, symmetric appearance, while relatively weaker wind zones remain on the left side (Figs. 4b,d).
317 The vertical cross-section clearly illustrates the structural changes that Henri underwent; it reveals a distinct calm wind zone
318 within the eyewall, extending up to 9-km level. Areas of strong wind speeds exceeding 24 m s^{-1} are relatively evenly distributed
319 relative to the centre, with the strongest winds located on the right side. The corresponding simulated vertical profiles and
320 horizontal distributions of wind speed at 1-km level at 00 UTC 21st and 22nd August 2021 are shown in Figs. 4e-p.

321 All three simulated storms reasonably capture the structural changes that Henri underwent, including the transition in wind
322 distribution from a wide, open, asymmetric pattern with strong wind zones on the right side observed at 00 UTC on 21st in TC-
323 RADAR to a more compact, closed, symmetric structure as it intensifies observed at 00 UTC on 22nd August in TC-RADAR.



324 However, the simulated storms noticeably overestimate intensity horizontally and vertically, especially the experiments ‘A’
325 and ‘AO.’ The fully coupled simulation ‘AOW’ notably mitigates the overestimation with better radial wind profiles at the 1-
326 km level along the line from A to B for both times (Fig. A1), and higher Pearson correlation coefficients (r) of 0.95 and 0.72,
327 respectively—the highest correlations among the three simulations at both times. For a more comprehensive examination, we
328 assess the wind distribution using probability density function (PDF) considering all available observation grid cells
329 horizontally and vertically within the 300 km x 300 km domain relative to the storm centre, from 0.5 km to 9 km above the
330 ground provided by TC-RADAR (Fig. 5). The PDF distribution clearly shows that all three simulated wind distributions skew
331 toward higher intensities compared to the observed data at both times. However, it is evident that ‘AOW’ reduces the
332 overestimation, particularly in the upper tail, indicating that ‘AOW’ improves the wind bias during the storm’s development.
333 While the TC-RADAR provides comprehensive observations in both horizontal and vertical dimensions, the lowest level of
334 TC-RADAR for this storm is 0.5-km above the ground. This height limits us to validate modelled winds at heights that
335 hurricanes pose actual risks to offshore infrastructure and human activities. Dropsonde observations from aircraft can bridge
336 this gap. Figure 6 shows the vertical cross-sections of observed and simulated wind speed along the blue line shown in Fig.
337 3d. Consistent with TC-RADAR observations at higher altitudes, the dropsonde observation also shows that the strongest
338 winds are on the eastern side, approximately 10 to 30 km from the storm centre, with intensity gradually decreasing toward
339 the edge. On the other hand, much weaker speeds are observed on the western side, ranging from -10 to -200 km (Fig. 6a).
340 The observed patterns are reasonably captured in all three simulations, though they are generally overestimated. The
341 azimuthally averaged vertical profiles of simulated wind speeds in the inner-eyewall (defined as region within $0.2 \leq r/RMW \leq 1$)
342 and the outer-eyewall ($2 \leq r/RMW \leq 2.5$) regions are also evaluated (Fig 7). In both the inner- and outer-eyewall regions, it is
343 evident that all three simulations overestimate wind speeds in the low troposphere (below 2 km). However, ‘AOW’ aligns
344 more closely with observations compared to the other two simulations in both the inner- and outer-eyewall regions. Notably,
345 in the outer-eyewall region, ‘AOW’ is much closer to the observed values. These insights are particularly relevant for offshore
346 wind resources, as accurate wind profiles at hub heights and below are crucial for optimizing turbine placement and enhancing
347 energy generation efficiency in storm prone areas. A better representation of wind profiles, especially in the low troposphere
348 and near the surface, not only helps in predicting potential impacts on the turbines but also informs better design and operational
349 strategies.

350



351

352

353

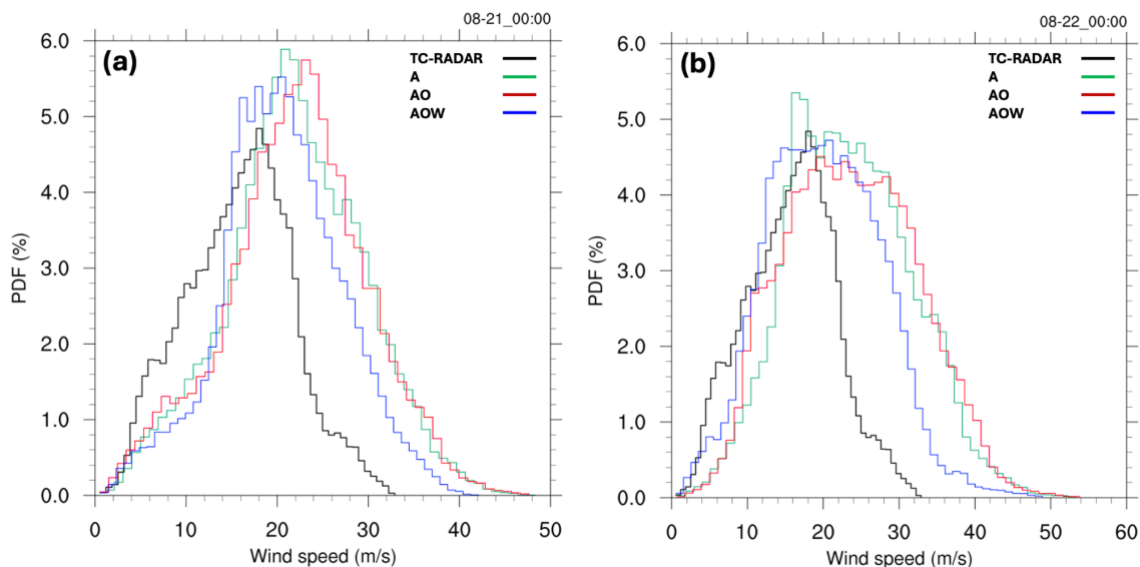
354

355

356

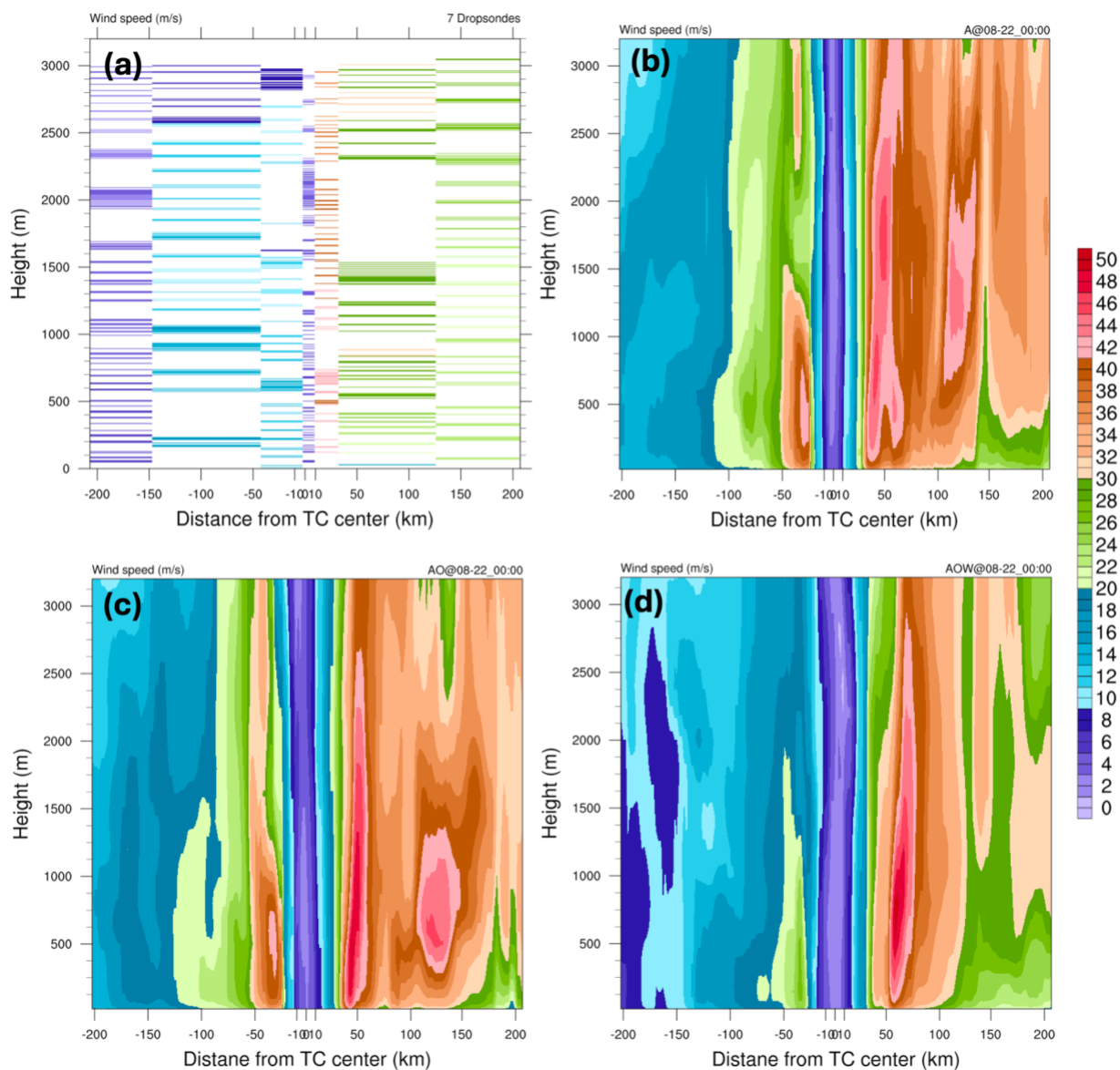
357

Figure 4. NOAA WP-3D airborne Doppler radar-observed (TC-RADAR) wind speeds at the 1-km level are shown in the first row, along with the corresponding model-simulated wind speeds for Hurricane Henri (2021) from the ‘A’ simulation (second row), ‘AO’ simulation (third row), and ‘AOW’ simulation (fourth row) at 00 UTC on August 21 (first and third columns) and 00 UTC on August 22 (second and fourth columns). The vertical cross-sections of wind speeds along the line from point A to B, indicated in the leftmost two columns, are presented in the rightmost two columns. All horizontal distributions are displayed in a 300 km × 300 km storm-centred coordinate.



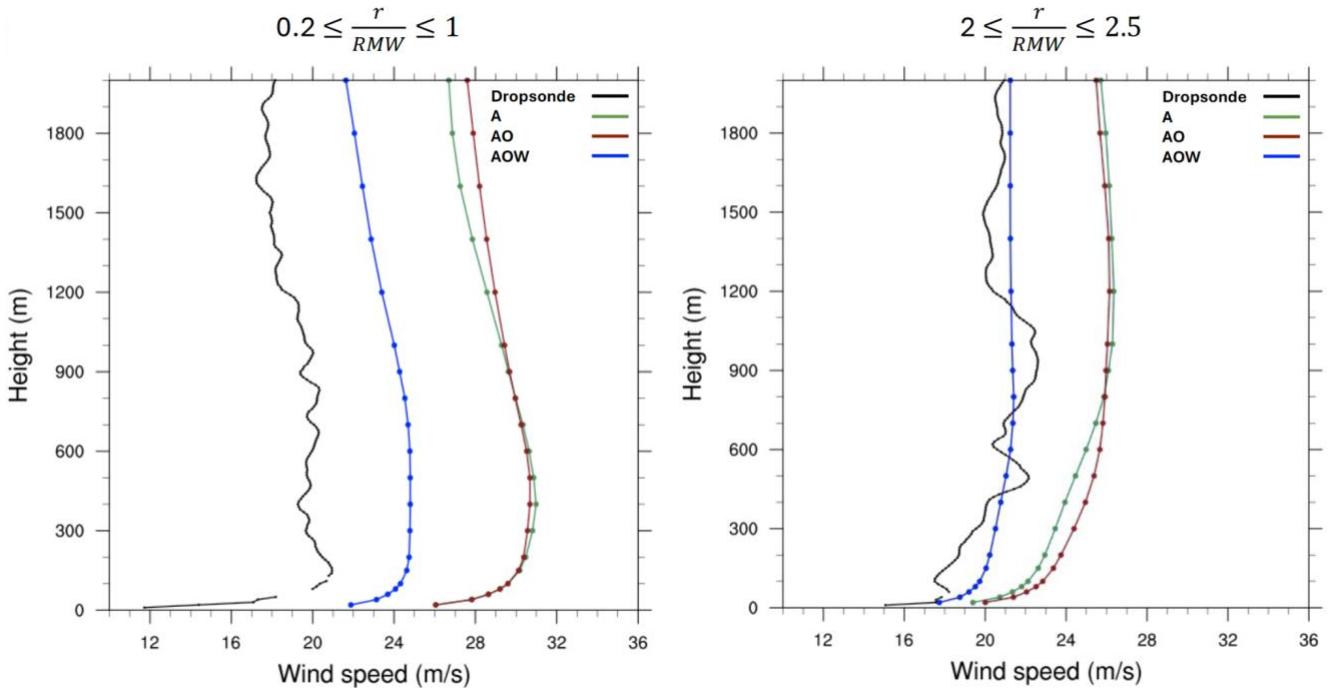
358
359
360
361

Figure 5. Probability density function of wind speed in a 300 km x 300 km storm-centered coordinate, considering vertical levels from 0.5 km to 9 km above the ground, for 00 UTC on 21 August (a) and 22 August (b) 2021. The data are derived from TC-RADAR (black lines), experiment ‘A’ (green lines), experiment ‘AO’ (red lines), and experiment ‘AOW’ (blue lines).



362

363 **Figure 6.** Vertical cross-sections of (a) observed wind speed along the locations of the seven dropsondes, shown as colored dots in
364 **Fig. 3(d).** The times of the first and last dropsondes are 23:23 UTC on 21 August and 00:11 UTC on 22 August, respectively.
365 **Corresponding cross-sections from (b) experiment 'A', (c) experiment 'AO', and (d) experiment 'AOW' are shown.**



366

367 **Figure 7. Vertical profiles of azimuthally averaged wind speed for dropsondes (black lines), experiment ‘A’ (green lines), experiment**
368 **‘AO’ (red lines), and experiment ‘AOW’ (blue lines). The vertical profiles are azimuthally averaged in the inner-eyewall region (left;**
369 **$0.2 \leq r/RMW \leq 1$) and the outer-eyewall regions (right; $2 \leq r/RMW \leq 2.5$) on 22nd August 2021.**

370 4.2 Sea Surface Temperature and Waves

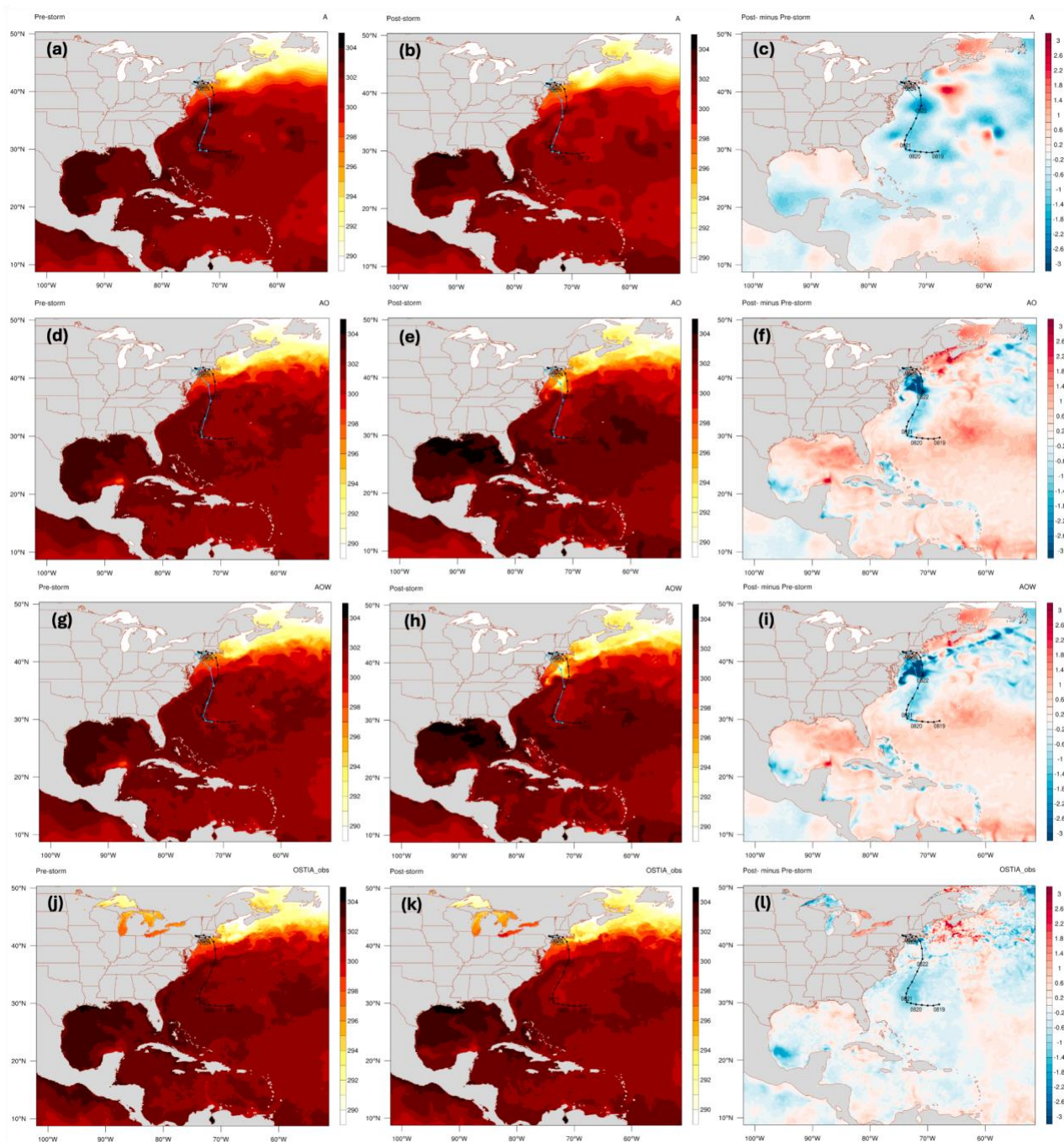
371 4.2.1 Sea Surface Temperature

372 Several factors influence TC intensity, with SST and ocean surface roughness being among the most important, as they directly
373 affect the heat and moisture available to fuel the storm (Zambon et al., 2014, 2021; Zhao et al., 2022). In our model
374 configurations, the primary difference between the simulations lies in the treatment of SST and sea surface roughness, which
375 ultimately impacts surface enthalpy and momentum fluxes through atmosphere-ocean interaction feedback. Therefore, we use
376 SST as both a primary indicator and a driving mechanism of storm intensity to analyse the differences in Henri’s intensity
377 modelled by the three experiments.

378 Figure 8 illustrates the distribution of SST over the entire simulation domain for all three simulations, along with OSTIA
379 observation at 12 UTC on 20th August (pre-storm) and 12 UTC on 23rd August (post-storm). The figure also shows the
380 differences of SST between post- and pre-storm periods. Overall, all three simulations reasonably represent the SST
381 distribution in both pre- and post-storm periods, effectively capturing the intensity and spatial extent of the Gulf Stream and
382 surrounding warm SST zones (Fig. 8). Notably, both ‘AO’ and ‘AOW’ simulations adequately resolve cooler SSTs along the
383 storm tracks, with comparable RMSEs and pattern correlations in comparison with SST in ‘A’ (Table 2). However, the two
384 coupled simulations tend to overestimate cooling as the storms approach the U.S. Northeast Coast (Fig. 8f,i,l).

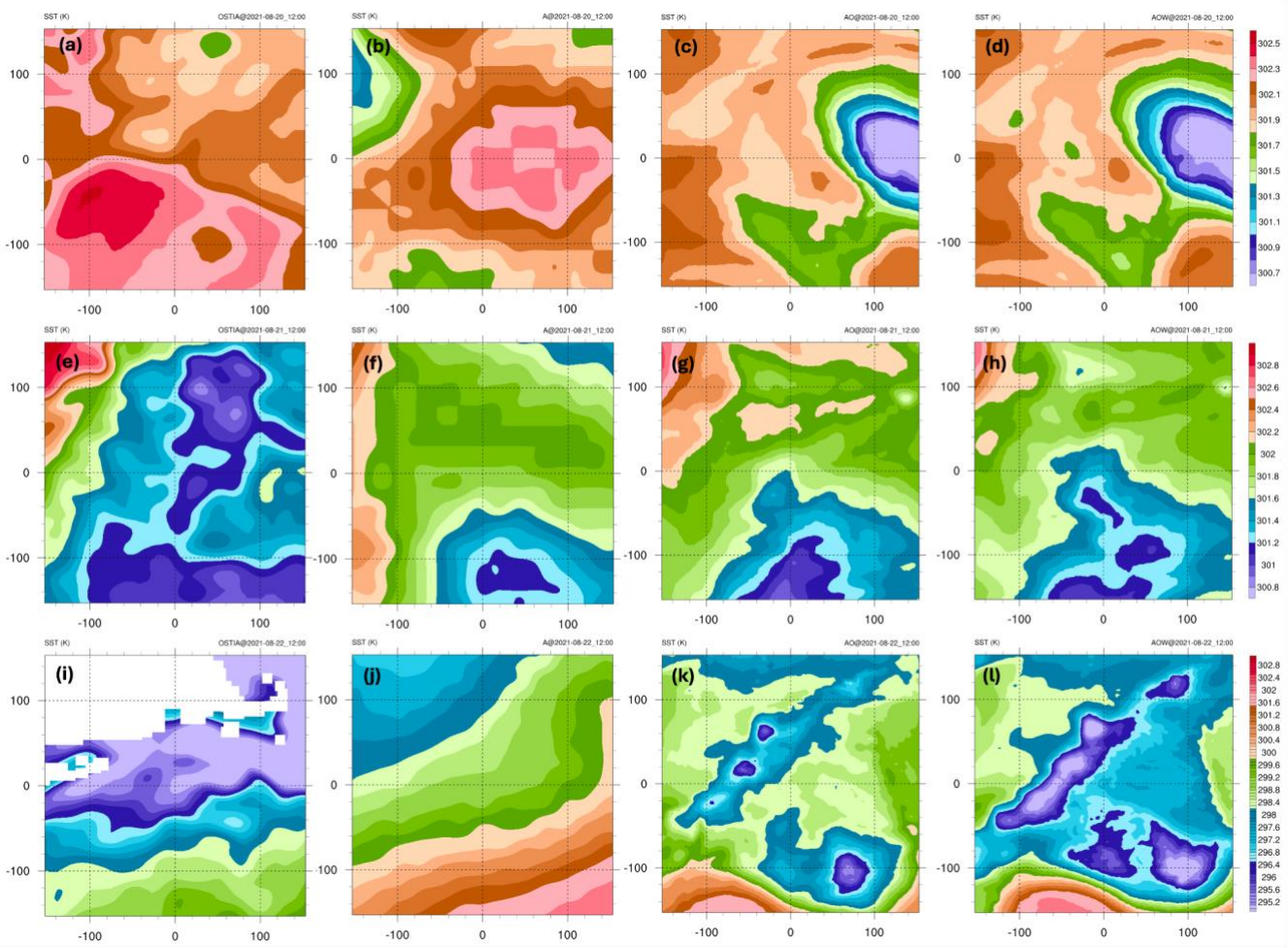


385 Figure 9 displays the distribution of SST for the four datasets in a 300 km x 300 km storm-centred at 24-hour intervals from
386 12 UTC on 20th August to 12 UTC on 22nd August. The area-averaged SST in the storm-centred coordinate is calculated and
387 OSTIA and listed in Table 3. At 12 UTC on 20th August, Henri turned northward and continued to strengthen with the aid of
388 relaxed wind shear and high SST associated with the Gulf Stream (Pasch, 2022; Fig. 9a). OSTIA well illustrates the warm
389 SST, with values exceeding 302.2 K (29.05 °C) on the southern side of the storm (Fig. 10i). However, none of the three
390 simulations accurately capture the southern warm SST distribution due to differences in their translation speeds and
391 corresponding locations, as well as biases in SST (Fig. 3a and 8-9). In addition, the two coupled simulations overpredict the
392 cold wakes on both southern and eastern sides of the storm (Figs. 9c-d), resulting in weaker minimum SLP compared to the
393 observation at this time (Fig. 3b). As the storm moved north-northeastward, the Gulf Stream and the surrounding warm waters
394 allowed it to deepen gradually, reaching its peak minimum SLP around 12 UTC 22nd August. It then weakened rapidly as it
395 interacted with land masses, making landfall in Rhode Island (Figs. 3 and 8). While the warm waters and cold wakes associated
396 with the storm are generally captured in all three simulations, the magnitude and spatial extent of the storm produced cold
397 wakes are mostly weaker, leading to an over-intensification of all simulated storms compared to the observation until they
398 make landfall (Figs. 9e-l). The overestimations are also partly due to the biases in track, making the simulated storms approach
399 the coast along different paths, which affect their intensity and interaction with the surrounding environment. Note that SST
400 in ‘A’ is updated by GFS reanalysis data at 6-hour intervals. Although the SST in GFS is derived from observation-based
401 reanalysis data, its distribution and magnitude differ from those of OSTIA (Fig. 8). This discrepancy likely arises from
402 variations in observational data sources and spatial resolution. OSTIA SST is generated using a combination of satellite
403 observations and in situ measurements (e.g., buoys, ships), offering high-resolution analysis at a 1/20° grid. In contrast, GFS
404 SST features a coarser resolution of 0.25° and predominantly relies on global ocean models and reanalysis datasets, which
405 may not incorporate the same observational data sources as OSTIA. Although all three simulations overestimate the intensity
406 of Henri, the experiment ‘AOW’ noticeably reduces the overestimation during the development as well as weakening stages,
407 as previously discussed. This might be due to the greater cooling of SST associated with wave-induced vertical mixing,
408 bringing cold water up to the surface consistent with prior studies (e.g., Wada et al., 2010; Zambon et al., 2014; Figs. 10d and
409 h).



410

411 **Figure 8.** SST comparisons for various experiments: ‘A’ (SST updated by GFS at 6-hour intervals, first row), ‘AO’ (atmosphere-
412 ocean model coupling, second row), ‘AOW’ (atmosphere-ocean-wave model coupling, third row), and OSTIA SST observation
413 (fourth row). The first column shows SST at 12 UTC on 20th August (pre-storm), the second column displays SST at 12 UTC 23rd
414 August (post-storm), the third column presents change in SST between pre-storm and post-storm. The black dots and lines indicate
415 the best track derived from IBTrACS. The light blue dots and lines depict simulated storm locations and tracks.



416

417

418

419

420

Figure 9. Distribution of SST in a 300 km × 300 km storm-centered coordinate at 12 UTC on August 20th (top row), 12 UTC on August 21st (middle row), and 12 UTC on August 22nd (bottom row). The first column shows SST derived from OSTIA, the second column presents SST values from ‘A’, the third column displays SST from ‘AO’, and the fourth column shows SST from ‘AOW’ simulation.

421

422

TABLE 2. Temporally averaged root mean square error (RMSE) and Pearson product-moment coefficient of linear correlation (r) for SST in each simulation compared to OSTIA SST observations from 12 UTC on 20th August to 12 UTC 23rd August, 2021.

Experiment	RMSE	Pattern Correlation
A	0.631	0.992
AO	0.564	0.991
AOW	0.577	0.990

423

424

425

TABLE 3. Spatially averaged SST (K) derived from A, AO, AOW, and OSTIA observation in a 300 km x 300 km storm-centered coordinate at 12 UTC 20 August, 12 UTC 21 August, and 12 UTC 22 August.

Experiment	08-20_12:00	08-21_12:00	08-22_12:00
A	302.01	301.81	299.37

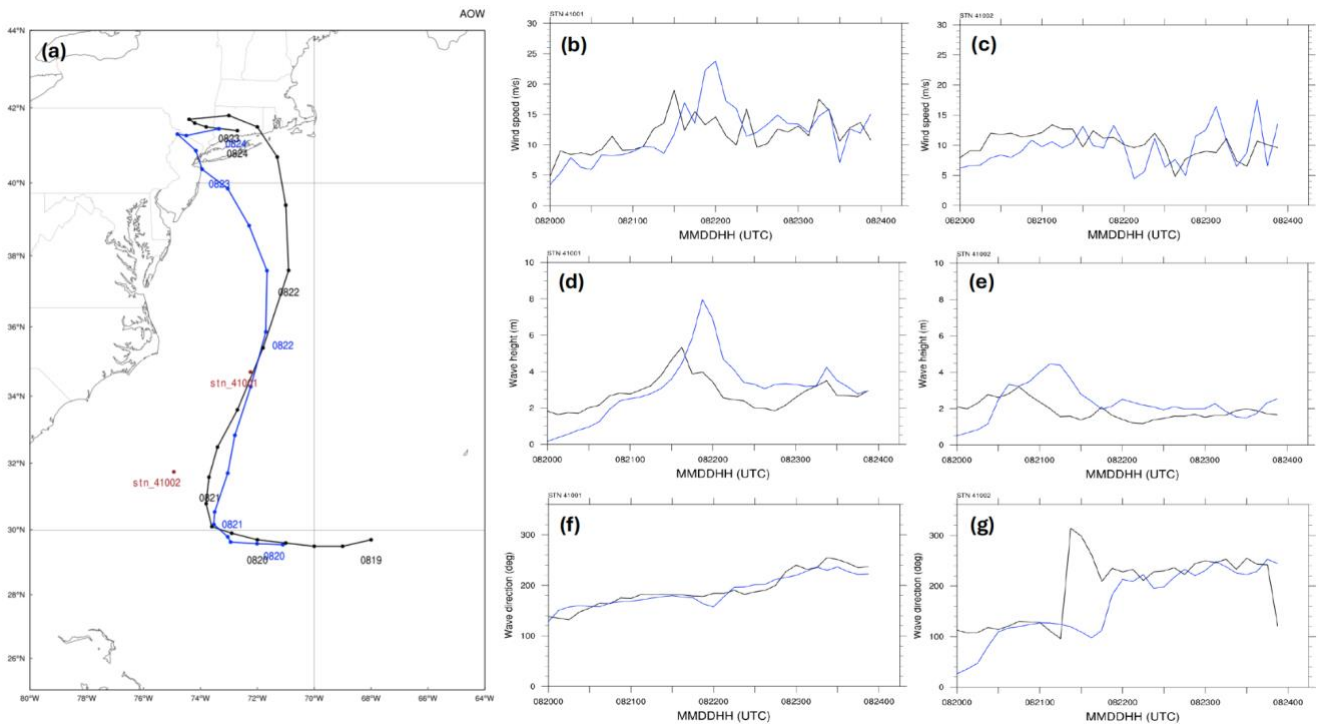


AO	301.79	301.83	298.47
AOW	301.76	301.70	297.70
OSTIA	302.15	301.43	296.76

426 **4.2.2 Ocean Surface Waves**

427 In this section, we examine the accuracy of modelled ocean surface waves throughout the evolution of Hurricane Henri at the
428 two NDBC buoys. During the storm’s main development stage, station 41001 experienced the passage of the eye and the high
429 winds and waves associated with the eyewall. Meanwhile, station 41002 was positioned about 120 km to the left of the storm’s
430 centre during its closest approach in the early development stage. The fully coupled experiment reasonably captures the general
431 temporal trends of wind speed at both locations (Fig. 10b-c). However, due to the slower translation speed of the modelled
432 storm, particularly from 06 UTC to 12 UTC on 21st August, the wind speed peaks are approximately 12 hours later than
433 observed at the two locations. Consequently, the wave peak times at both locations are similarly delayed. The modelled
434 magnitude of significant wave height is about 1-2.5 m higher than observed during peak times (Figs. 10d-e). At station 41001,
435 the difference in wind speed between observed and modelled ones generally accounts for the difference in significant wave
436 height. On the other hand, at station 41002, an additional factor that may contribute to the difference between observed and
437 modelled significant wave height is the faster translation speed following the storm’s slow movement from 06 UTC on 20th to
438 00 UTC on 21st August. Specifically, the translation speed of modelled storm is approximately 6.3 m s⁻¹, whereas the observed
439 speed is approximately 4.8 m s⁻¹ during the period from 00 UTC to 06 UTC on 21st August. On the right side of the storm’s
440 path, the wind speed is amplified because the storm’s forward motion adds to the wind speed. In this context, a faster moving
441 storm can lead to stronger wind forcing, which increases wave energy and promotes greater wave growth, resulting in higher
442 waves (Chen et al., 2013). While the fully coupled experiment effectively captures the wave direction at station 41001, it does
443 not resolve the sharp directional change observed at station 41002 between 06 UTC and 09 UTC on 21st August. This lack of
444 sharp directional change could be due to the model’s increased wavelength and height as previously described, which prevent
445 the observed rapid shifts in wave direction. Despite some biases in wave features, including magnitude and timing of peak
446 wave height, the overall performance of the modelled waves at the two NDBC locations are reasonable and demonstrates the
447 model’s ability to capture general trends in storm-induced wave behaviour during Hurricane Henri.

448
449



450

451

452

453

454

455

456

457

458

459

460

461

462

463

464

465

466

467

468

Figure 10. Comparison of ‘AOW’ simulated in blue (a) track, (b)-(c) wind speed (m/s), (d)-(e) significant wave height (m), and (f)-(g) wave direction of Hurricane Henri with the observations in black from station 41001 (b),(d),(f) and station 41002 (c),(e),(g) during the period from 00 UTC on 20 August to 00 UTC on 24th August 2021.

4.3 Mechanisms Underlying the Improvement in the Fully Coupled Experiment

So far we have learned that, compared to experiments ‘A’ and ‘AO’, ‘AOW’ not only reduces the overestimation of storm intensity (represented by the minimum SLP, Fig. 3) but also improves storm-scale wind structure (Fig. 4) and wind speed distribution (Fig. 5) compared to observations from the near surface to the upper troposphere for Hurricane Henri (2021). To examine the mechanisms behind these improvements, we first analyse SST and surface enthalpy flux of ‘AOW’ and compare them with those of ‘AO’ to examine ocean surface wave-induced processes and their influence on the evolution of Henri. We opted out of experiment ‘A’ in this analysis, as it is an atmosphere standalone simulation and does not consider atmosphere-ocean interactions.

Since both ‘AO’ and ‘AOW’ simulations have very similar storm tracks and comparable translation speeds, we are able to isolate the surface properties, including effects of SST, enthalpy flux, and surface roughness length on storm dynamics and evaluate how these factors contribute to differences in storm intensity and evolution. First, from a momentum transfer perspective, ocean surface waves characterize the surface roughness length (Z_0) of the ocean and regulate the exchange of momentum, in addition to heat and moisture, between the atmosphere and ocean. Without coupling the waves and the atmosphere, Z_0 or drag coefficient (C_d) is calculated solely based on wind speed (e.g., Charnock formulation). As a result,



469 ‘AO’ might not accurately capture the dynamic interactions between the lower atmosphere and ocean surface during TCs
470 where wave effects and varying sea surface conditions significantly impact momentum transfer and overall system evolution.
471 We chose the time of 12 UTC on 22nd August 2021 to investigate these interactions in detail, focusing on how the inclusion of
472 wave dynamics in the fully coupled experiment ‘AOW’ alters the estimate of surface roughness length and the subsequent
473 effects on momentum and heat exchange during the hurricane's intensification phase. The timing is particularly significant, as
474 it marks the moment when the simulated storms from both ‘AO’ and ‘AOW’ reached their peak minimum SLP, occurring
475 about 12 hours prior to landfall. As shown in Fig. 11, ‘AO’ and ‘AOW’ simulate very different distributions of Z_0 , clearly
476 demonstrating that ‘AO’ is solely a function of surface wind speed, while the Z_0 distribution of ‘AOW’ is distinct from the
477 surface wind distribution. This implies that wave dynamics play a crucial role in shaping Z_0 (Figs. 11a,b,e,f).

478 The impact of including ocean surface waves is not limited to just the representation of Z_0 . ‘AOW’ is associated with stronger
479 winds, but lower SST, and surface enthalpy flux compared to ‘AO.’ The primary process responsible for cooling SST under
480 TCs is ocean vertical mixing, as discussed. During such events, the storm's surface winds create stress on the ocean surface
481 through friction, generating ocean currents in the mixed layer and momentum flux at the bottom of the atmosphere, leading to
482 evaporation from the ocean surface. In addition to the evaporative cooling, vertical velocity shear of the currents in the upper
483 ocean leads to turbulence, which mixes and entrains colder water from below the mixed layer, and reduces SST (e.g., Zhou et
484 al., 2023). This process is represented in both ‘AO’ and ‘AOW.’ However, the inclusion of wave dynamics in ‘AOW’ adds
485 additional vertical mixing through the following processes: the storm's surface winds build waves at the sea surface, and the
486 momentum transfer from the atmosphere to the ocean grows and propagates these waves. When the waves break, momentum
487 is transferred downward into the ocean currents, leading to vertical shear and thus vertical mixing. On the other hand, mixing
488 induced by non-breaking waves penetrates much deeper, leading to a further reduction in SST, as previously discussed. This
489 additional wave dynamics included in ‘AOW’ results in greater cooling in SST, leading to a reduced surface enthalpy flux
490 compared with ‘AO’ (Fig. 11). The reduced Z_0 in ‘AOW’ corresponds to a lower C_d , meaning that the roughness—primarily
491 due to the inclusion of waves—is less, which leads to higher wind speeds at the surface.

492 An important question remains regarding the discrepancy between minimum SLP and maximum wind speed in ‘AO’ and
493 ‘AOW.’ Specifically, while ‘AO’ shows more intense (i.e., lower) minimum SLP than ‘AOW’, its maximum wind speed is
494 weaker compared to ‘AOW’ at this time (12 UTC on 22nd August; Fig. 3b-c and Figs. 11a-b) despite being linked to greater
495 surface enthalpy and momentum flux. As discussed, ‘AO’ is linked to higher Z_0 due to the absence of active wave dynamics
496 in the simulation, resulting in reduced surface wind speeds from increased frictional drag. This can lead to stronger subgradient
497 winds, where the actual wind speed is lower than what would be expected from the gradient wind balance. The relationship
498 between tangential circulation and radial inflow in the boundary layer is described by the agradient force (Montgomery and
499 Smith, 2014; Smith et al., 2009), which is defined as the difference between pressure gradient force and the sum of centrifugal
500 and Coriolis forces in the form of

501

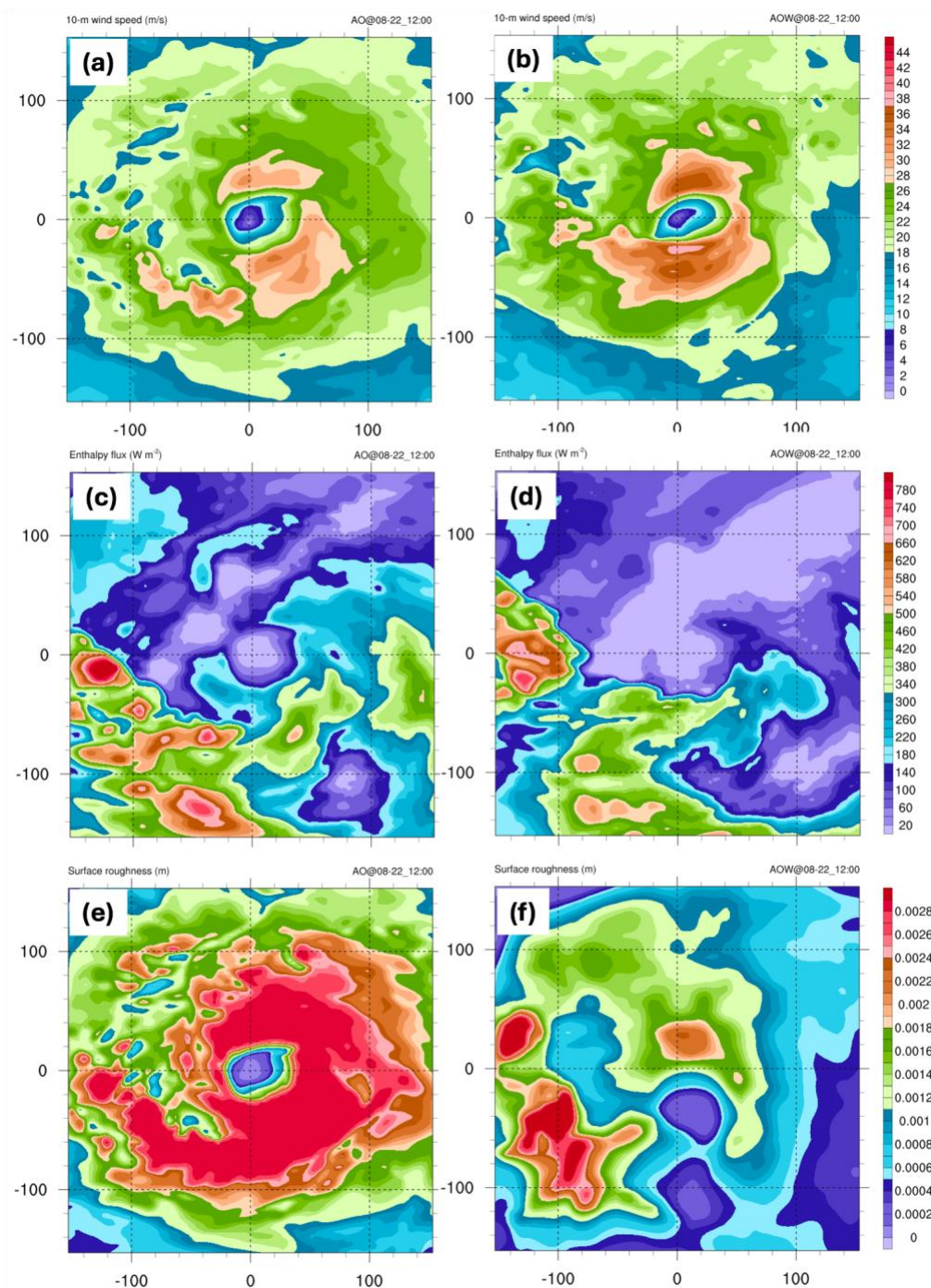


502
$$\text{Agradient Force (AF)} = -\frac{1}{\rho} \frac{\partial p}{\partial r} + \frac{V_t^2}{r} + fV_t \quad (3)$$

503

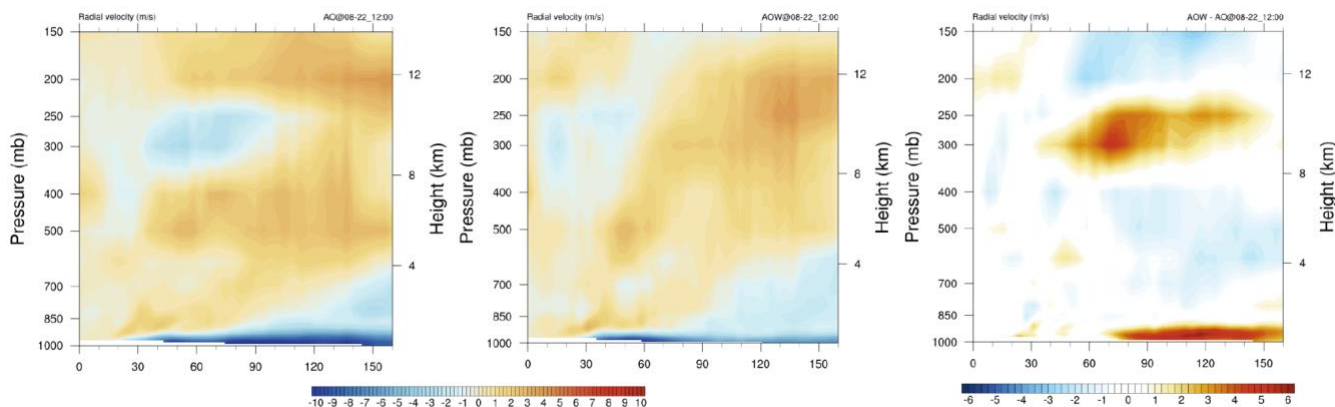
504 where P is air pressure, r represents radius from the TC centre, V_t refers to tangential wind speed, and ρ is air density. Near
505 the surface, both ‘AO’ and ‘AOW’ deviate from gradient wind balance due to the effects of friction. Friction reduces the
506 tangential wind speed, thereby weakening both Coriolis and centrifugal forces, while the pressure gradient force remains
507 unchanged (negative agradiant force: $AF < 0$). This imbalance results in a net inward force, driving inflow in the lower
508 atmospheric layers (the secondary circulation). The magnitude of this inflow can be seen as an indicator of the deviation from
509 the gradient wind balance, with stronger inflow corresponding to a greater degree of subgradient wind. The azimuthally
510 averaged radial wind speed clearly shows that the enhanced inward flow towards the storm centre in the boundary layer in
511 ‘AO’ compared with the ‘AOW’ (Fig. 12). In the boundary layer, stronger radial inflow transports additional absolute angular
512 momentum (AAM) toward the storm’s core, although friction disrupts the perfect conservation of AAM. As air moves inward,
513 its radius decreases, causing tangential wind speeds to increase (as per the conservation of AAM). While friction within the
514 boundary layer slows the tangential winds, the winds still strengthen near the core due to the influx of air masses. This increase
515 in wind speed amplifies the outward centrifugal force, which is primarily counteracted by a greater inward pressure gradient
516 force, resulting in a lower central pressure in the storm’s core. In ‘AO’, even though the simulated storm is associated with
517 stronger radial inflow through the process described above, the tangential winds along the storm centre are unable to increase
518 relative to ‘AOW’ due to the additional friction effects over the ocean (Figs. 11 and 12). This extra friction in ‘AO’ is caused
519 by an unrealistically calculated , which is only a function of surface wind speed. As surface wind speeds up, it generates more
520 friction or drag on the ocean surface, which can further disrupt the conservation of AAM in ‘AO.’ As a result, the additional
521 frictional dissipation of AAM in ‘AO’ leads to a reduction in the amount AAM available to drive wind’s acceleration.
522 Consequently, the wind speeds in ‘AO’ do not increase as much as expected despite the enhanced radial inflow. This explains
523 the slower rate of intensification observed in ‘AO’ compared with its fully coupled counterpart, ‘AOW’ during the period from
524 06 UTC to 12 UTC on 22nd August. Note that as both simulated storms move through the baroclinic zone at this time, they
525 may experience vertical wind shear. This can disrupt the typical inflow-outflow structure of tropical storms, leading to
526 anomalous inflow at upper levels observed in Fig. 12.

527



528

529 **Figure 11.** Distribution of (a)-(b) 10-m wind speed (m s^{-1}), (c)-(d) surface enthalpy flux (W m^{-2}), and (e)-(f) surface roughness length
530 (m) derived from the experiment ‘AO’ (left column) and the experiment ‘AOW’ (right column) at 12 UTC on 22nd August 2021. All
531 distributions are displayed in a $300 \text{ km} \times 300 \text{ km}$ storm-centred coordinate.



532

533 **Figure 12. The azimuthally averaged radial wind speed (m s^{-1}) for the (a) experiment ‘AO’, (b) experiment ‘AOW’, and (c) difference**
534 **between ‘AOW’ and ‘AO’ at 12 UTC on 22nd August 2021.**

535 **5 Implication for Potential Risks to Offshore Wind Energy**

536 As the global demand for renewable energy continues to rise, offshore wind energy has emerged as a promising solution in the
537 transition toward sustainable power generation. However, this opportunity comes with potential risks, particularly from TCs,
538 which can generate extreme sea surface wave conditions, high wind speeds, and significant shear and veer between the ocean
539 surface and hub heights (Wang et al., 2024a,b). Loads on offshore structures can arise from both aerodynamic and
540 hydrodynamic forces and both act simultaneously on a turbine during a TC. In a design context, factors such as sustained wind
541 speed, its relationship to wind gusts, the assumed vertical profile (shear) of the boundary layer, and wave heights and periods
542 are crucial for calculating loads and are generally well understood. However, properties of the wind profile, including veer, as
543 well as the temporal variability and directional dependence of wind and wave loads, remain less understood and are often not
544 fully accounted for (Sanchez Gomez et al., 2023; Wang et al., 2024b).

545 **5.1 Wind Veer**

546 Wind veer is defined as the rate of change in wind direction with altitude (e.g., Churchfield and Sirmivas, 2018; Sanchez Gomez
547 et al., 2023). Although the International Electrotechnical Commission (IEC) standards outlines the atmospheric conditions for
548 weather extremes, including TCs, to guide the design of onshore (61400-1 IEC, 2019a) and offshore (61400-3 IEC, 2019b)
549 wind turbines, wind veer is not accounted for in current design specifications (Sanchez Gomez et al., 2023). This omission
550 remains despite its potential on turbine performance (Bardal et al., 2015; Gao et al., 2021) and loads (Churchfield and Sirmivas,
551 2018; Kapoor et al., 2020; Robertson et al., 2019; Sanchez Gomez et al., 2023). Large changes in wind direction with increasing
552 altitude, driven by extreme events, can be destructive for wind turbines. For instance, a disruption in the grid connection caused
553 by these extreme events may prevent the turbines from yawing into the wind, or the wind direction may change too quickly
554 for the yaw control system to respond effectively, resulting in increased mechanical loads on the turbine components and



555 potential damage to the structure. To evaluate the wind veer simulated by ‘A’, ‘AO’, and ‘AOW’ simulations, we estimated
556 wind veer by calculating the difference in wind direction at multiple hub heights ranging from 100 m to 200 m in 10-m intervals
557 relative to the bottom ($z = 30$ m) of the turbine rotor layer. These results were then compared with dropsonde observations at
558 three different locations relative to the storm centre (~91 km to the left: yellow circle - called point A, ~40 km to the right:
559 green circle - called point B, and ~104 km to the right: red circle - called point C), as shown in Fig. 3d.

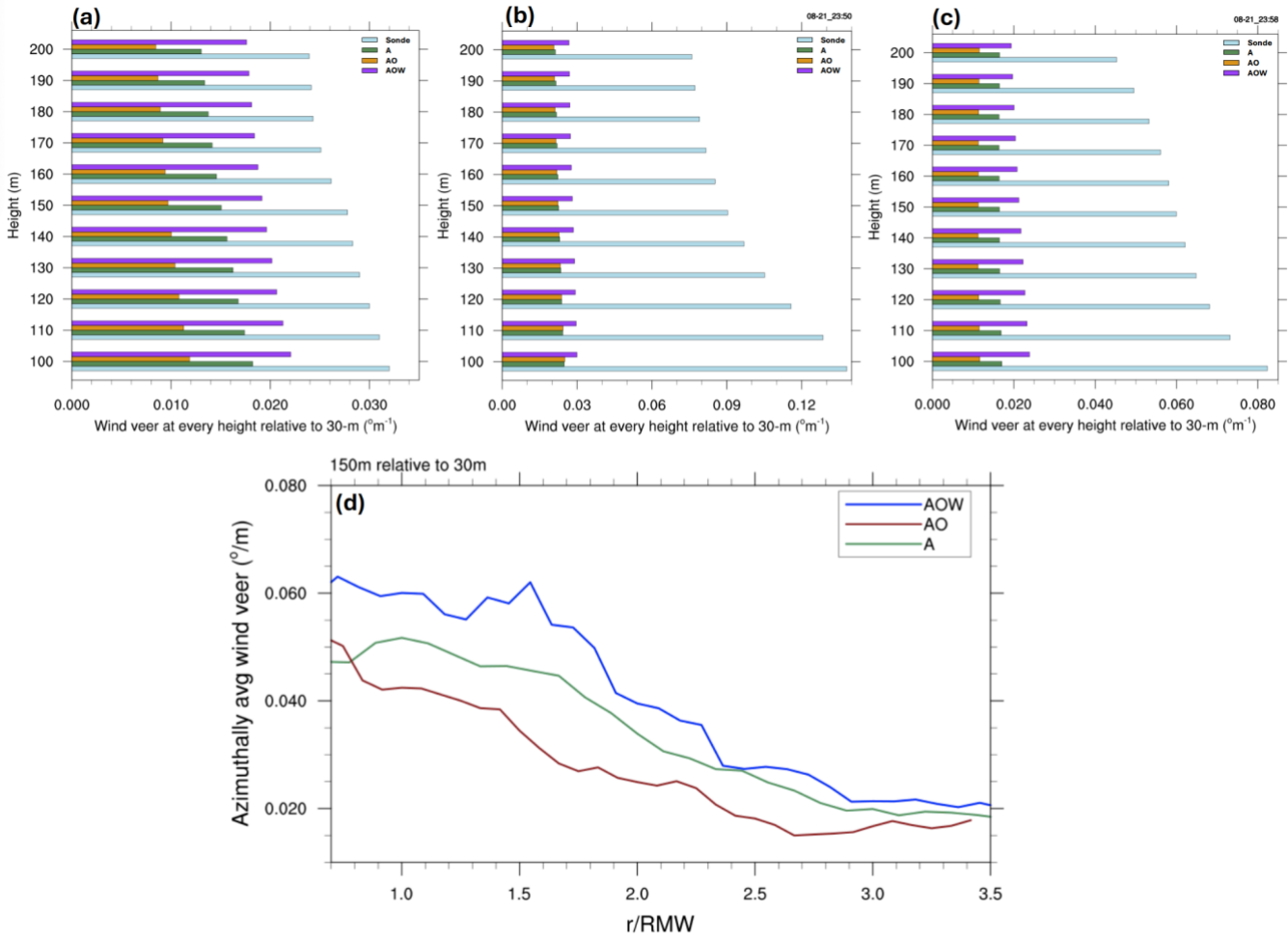
560 Firstly, the observations show that wind veer varies along the radius of the storm, with the veer noticeably increasing as it
561 approaches the centre of Henri around 00 UTC on 22 August. For example, at 150 m hub height, wind veer is $0.028^\circ/\text{m}$ at
562 point A (to the left of the centre), $0.09^\circ/\text{m}$ at point B (the closest point to the centre), and $0.06^\circ/\text{m}$ at point C (to the right of the
563 centre). In addition, it is apparent that wind veer is greater on the right side of the storm compared to its left side counterpart
564 at all hub height levels (Figs. 13a-c). All three simulations significantly underestimate the wind veer, especially on the right
565 side of the storm (Figs. 13b-c). Furthermore, the greater veer observed on the right side of the storm in the dropsonde data is
566 not clearly captured in any of the simulations. Nevertheless, all three simulations do reasonably capture the general trend that
567 wind veer increases as it approaches the centre of the storm. Azimuthally averaged wind veer at 150 m relative to 30 m at 00
568 UTC on 22nd August, shown in Fig. 13d, clearly displays that the wind veers associated with the simulated storms gradually
569 decrease with radius in all three simulations. Among the three simulations, ‘AOW’ better matches the magnitude of the veer
570 at all levels at the three dropsonde locations although it still largely underestimates the values (Fig. 13). The largest veer across
571 the radius is seen in ‘AOW,’ consistent with the Figs. 13a-c.

572 Wind veer and shear can be influenced by several factors, with atmospheric stability, surface friction, and subsequent dynamic
573 and thermodynamic processes, such as both mechanical- and buoyancy-driven turbulence and vertical mixing (e.g., Englberger
574 and Lundquist, 2020; Murphy et al., 2020), all of which play key roles. For example, in stable atmospheric conditions, wind
575 veer and shear are typically more pronounced within the boundary layer, as stratification inhibits vertical mixing. In contrast,
576 under unstable conditions, enhanced turbulence promotes mixing, which can reduce the magnitude of wind veer and shear by
577 redistributing momentum. Additionally, surface friction slows near-surface winds, reducing their speed and altering their
578 direction, which creates a vertical gradient in wind speed and direction that contributes to wind veer and shear. In the light of
579 this, we examine these factors to understand how the three simulations differ in simulating these properties and how they affect
580 the representation of wind veer. Over the ocean, surface enthalpy flux represents the heat and moisture exchanged at the
581 atmosphere-ocean interface, with a lower flux suggesting a more stable lower boundary layer, while a higher flux is associated
582 with a less stable one. Regarding turbulence, turbulent kinetic energy (TKE) is commonly used as a proxy for turbulence in
583 the atmospheric boundary layer, representing the energy associated with turbulent motions. Thus, we use TKE to assess the
584 intensity of turbulence in the simulated storms. Figure 14 indicates horizontal distributions of surface roughness length, surface
585 enthalpy flux, and TKE at 30-m above the ground for all three simulations at 00 UTC on 22nd August. Consistent with our
586 previous findings, Z_0 in ‘A’ and ‘AO’ exhibit similar magnitudes and distributions, as both are driven by surface wind. In
587 contrast, Z_0 in ‘AOW’ is significantly weaker and displays a distinct spatial distribution, characterized by ocean wave processes
588 (Figs. 14a-c). Similarly, the surface enthalpy flux in ‘AOW’ is the weakest among the three, aligning with our previous findings

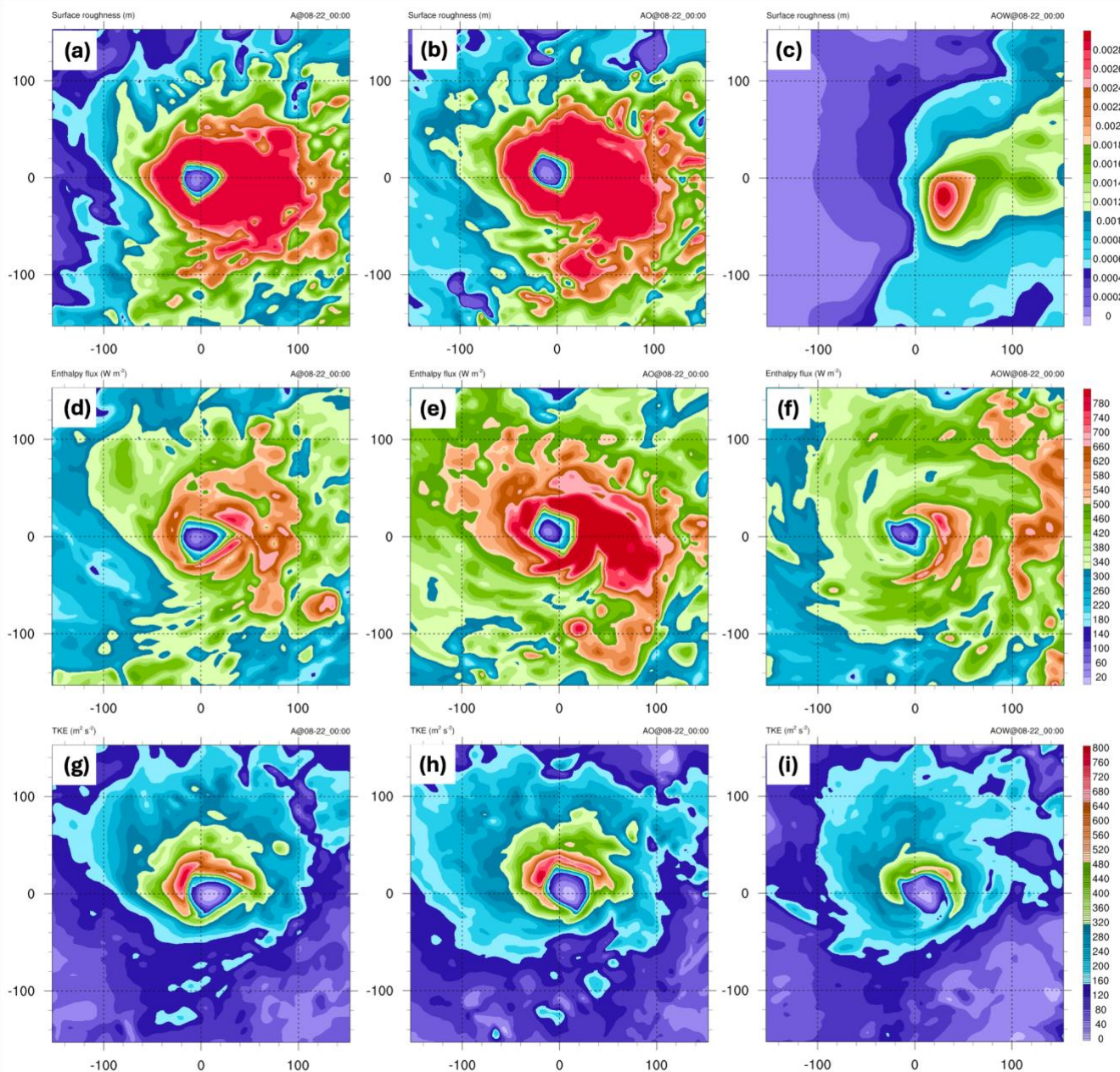


589 (Figs. 14d-f). In other words, ‘AOW’ is in a condition where decreased surface roughness and weaker surface enthalpy flux
590 act to suppress turbulent mixing. In relatively unstable atmospheric conditions, such as in ‘A’ and ‘AO,’ turbulence is more
591 pronounced due to buoyancy-driven mixing, which tends to redistribute momentum more evenly. Further, stronger Z_0 leads to
592 greater velocity shear between the atmosphere near the surface and above. This shear creates turbulent eddies that mix the
593 atmosphere. Therefore, more surface friction implies that the wind near the surface slows down more, creating stronger
594 turbulence that mixes the boundary layer. Figure 14 supports this idea, demonstrating that the experiments ‘A’ and ‘AO’ are
595 associated with greater surface enthalpy, stronger Z_0 , and higher TKE compared to those in ‘AOW.’ Strong turbulence
596 generated by both mechanically and thermodynamically tends to reduce wind veer by mixing momentum, while weaker
597 turbulence likely allows the veer to persist within the boundary layer (e.g., Sanchez Gomez and Lundquist, 2020; Stull 1988).
598 Thus, the weaker turbulence linked to the lower Z_0 in ‘AOW’ may restrict vertical mixing near the hub heights and below,
599 allowing the wind veer to remain more pronounced and closer to the observed values compared to the other two simulations.
600 It is important to note that the 3 km grid spacing used in the atmospheric model is still too coarse to accurately resolve fine-
601 scale turbulence processes. For instance, Li et al. (2021) highlighted that mesoscale models are incapable of properly capturing
602 small-scale features such as roll vortices, which are large turbulent eddies commonly found in a hurricane's boundary layer.
603 Furthermore, Müller et al. (2024) discussed how the lower wind veer values simulated in mesoscale modeling during Typhoon
604 Megi, compared to those reported by Sanchez Gomez et al. (2023), could be attributed to the higher resolved wind veer
605 variability in large eddy simulations (LESs). This limitation likely contributes to misrepresenting wind veer magnitude
606 (underestimations) in all three simulations when compared to the observations. Nevertheless, this finding underscores the
607 ability to capture critical atmosphere-ocean interactions, such as cold wakes, momentum transfer, surface stress, and boundary
608 layer dynamics, particularly in the context of wind veer assessment. This suggests that relying solely on atmospheric-only
609 models to quantify wind veer, as previously studied, may lead to inaccuracies and underestimations, underscoring the
610 importance of incorporating atmosphere-ocean-wave interactions in future simulations.

611
612



613
 614 **Figure 13.** Wind veer at multiple hub heights (ranging from 100 m to 200 m in 10-m intervals) relative to the bottom of the turbine
 615 rotor layer ($z = 30$ m) for (a) point A, (b) point B, and (c) point C. Point A is represented by a yellow dot, point B by a green dot, and
 616 point C by a red dot in Fig. 3d. (d) Azimuthally averaged wind veer ($^{\circ} \text{m}^{-1}$) for the experiments ‘A’, ‘AO’, and ‘AOW’ at 00 UTC on
 617 22nd August 2021. In (d), RMW denotes the radius of maximum wind, and r represents the radius relative to the storm centre.



618

619 **Figure 14.** Distribution of surface roughness length (m; upper panel), surface enthalpy flux (W m^{-2} ; middle panel), and turbulent
620 kinetic energy ($\text{m}^2 \text{s}^{-2}$; middle panel) for the experiments ‘A’ (left column), ‘AO’ (middle column), and ‘AOW’ (right column) are
621 shown at 00 UTC on 22nd August 2021.

622 5.2 Wind-Wave Misalignment

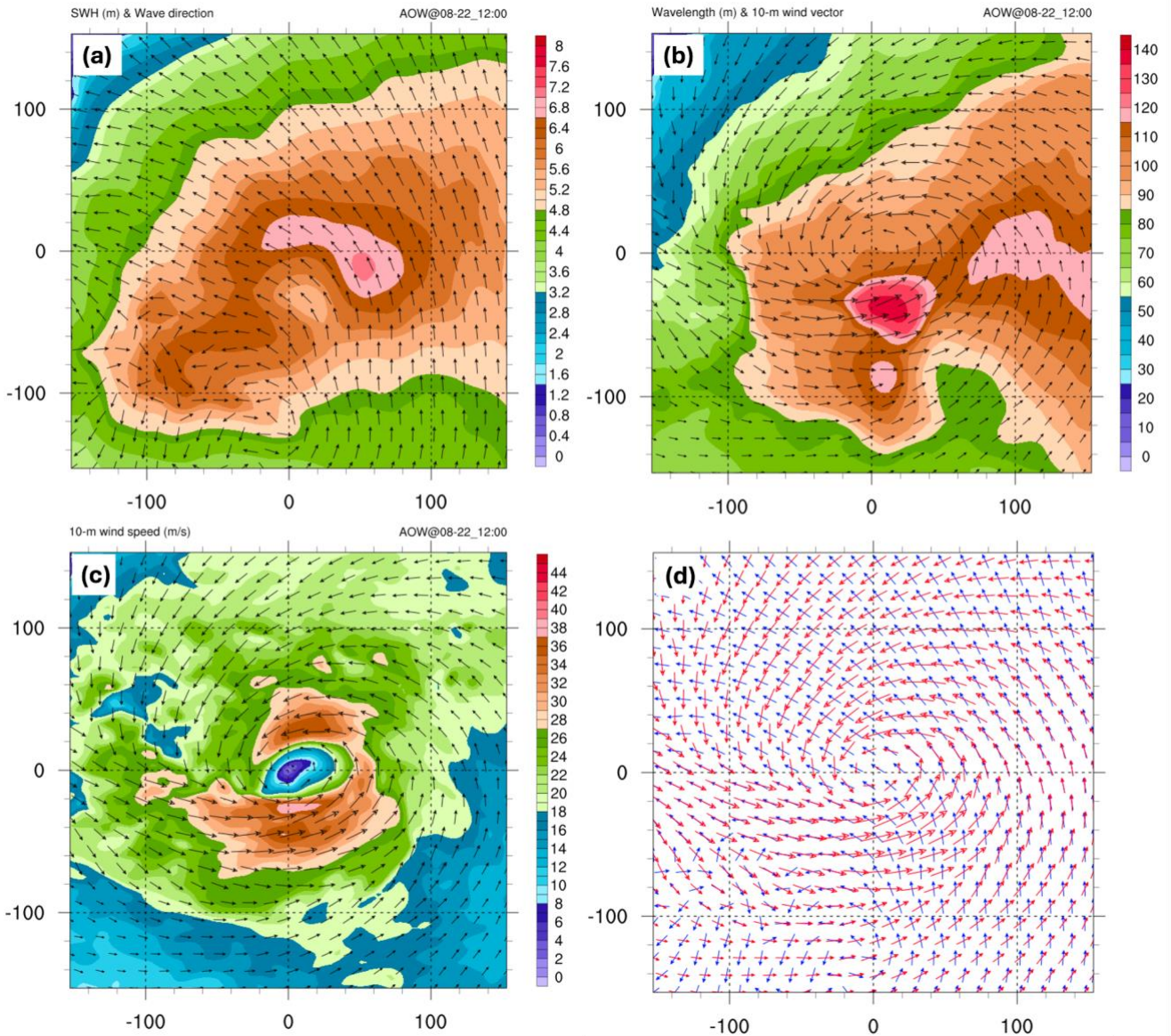
623 Wind-wave misalignment is another critical risk for offshore infrastructure that atmospheric-only models cannot estimate given
624 the lack of interaction between the atmosphere and ocean surface. Wind-wave misalignment can cause increased structural



625 loads on offshore wind turbines (discussed below), leading to fatigue damage and reduced operational lifespan. Figure 15
626 displays ocean surface wave information, including significant wave height, wave direction, and wavelength and 10-m wind
627 vector associated with the simulated in ‘AOW’ at 12 UTC on 22nd August. Previous studies have shown that the storm-induced
628 wave field around a hurricane is asymmetric, with the highest waves, as measured by significant wave height, typically
629 observed in the front-right quadrants of the storm (e.g., Chen et al., 2013; Wright et al., 2001). This typical characteristic is
630 also evident in our simulation, showing the highest significant wave heights in the right and front-right quadrants (Fig.15a).
631 Henri was heading northwest at 12 UTC on 22nd August 2021. In a moving storm, the waves to the right of the storm tend to
632 grow over time (Chen et al., 2013). This happens because the waves on the right side have a longer distance to travel and grow,
633 compared to the waves on the left side of the storm (Figs. 15a-b). In addition, directional misalignment of winds and waves is
634 evident on all sides of the storm, except the right side, consistent with prior study (Chen et al., 2013; Figs. 15d). This
635 misalignment is clearly represented in Fig. C1, which illustrates the time series comparison between surface wind direction
636 and mean wave direction at two NDBC buoy stations, 41002 and 41002. The figure highlights how the wave directions deviate
637 from the wind direction, as clearly observed in both NDBC buoys and the ‘AOW’ simulation, indicating complex interactions
638 at play.

639 These findings have significant implications for offshore wind energy operations and maintenance. When wind and wave
640 directions are not aligned (i.e., when they come from different directions), this creates substantial relative motion between
641 different parts of the wind turbine, specifically between the root (base) and the hub. This misalignment can lead to increased
642 movement or strain between these components. In contrast, when wind and waves are aligned, they combine in a way that
643 generates the highest impact velocities. This indicates that the forces acting on the turbine are stronger when the wind and
644 waves are moving in the same direction. In such conditions, with the two aligned, the turbine faces more severe impacts and
645 is at a higher risk of failure. Some studies have examined wind fields brought by TCs and their impacts on offshore wind
646 turbines (e.g., Sanchez Gomez et al., 2023; Wei et al., 2017; Itiki et al., 2023). However, most of these studies use either
647 atmospheric only models or empirical, parametric models that do not fully capture the complex interactions between wind and
648 wave forces during extreme events. This limitation makes it challenging to accurately predict the operational risks faced by
649 offshore turbines located in the hurricane belt. To assess this aspect, the models that incorporate atmosphere, ocean, and waves
650 components, are essential. Our fully coupled model with the three components can provide a realistic representation of wind
651 and wave behaviours, helping to predict wind-wave misalignment effectively. This allows for better assessment of the forces
652 acting on offshore wind turbines, enabling more informed design decisions and improved operational strategies to enhance the
653 longevity and reliability of wind turbine infrastructure.

654



655

656 **Figure 15.** The fully coupled model simulated the following at 12 UTC on 22nd August 2021: (a) significant wave height (shaded; in
657 meters) and wave propagation direction (vector), (b) mean wavelength (shaded; in meters) and 10-m wind (vector; in m/s), (c) 10-m
658 wind speed (shaded; in m/s) and wind vector (in m/s), and (d) wave propagation direction vector (blue) and 10-m wind vector (red).
659 The figures are displayed in a 300 km by 300 km storm-centered coordinate system. A reference wind vector of 20 m/s is shown in
660 panels (b) and (c).

661 6 Summary and Discussion

662 In this study, we developed a fully coupled modelling system (C-WFS) utilizing WRF, FVCOM, and SWAN to realistically
663 capture atmosphere-ocean-wave feedback on TC development and explore its implications for offshore infrastructure, such as



664 offshore wind turbines. We evaluated the performance of this coupled modeling system using Hurricane Henri (2021), selected
665 for its impact to the densely populated U.S. Northeast and nearby offshore wind lease area, as well as the extensive airborne
666 observations available. Three experiments with increasing complexity in atmosphere-ocean-wave coupled exchange
667 processes—'A', 'AO', and 'AOW'—were conducted and validated against a diverse range of observations, including IBTrACS,
668 airborne Doppler radar, dropsonde data, as well as both in-situ and satellite-based SST and wave measurements. The results
669 show that, while all simulated storms overestimate intensity in terms of minimum SLP, the fully coupled simulation 'AOW'
670 reduces this overestimation during both the development and weakening stages. Improvements are also evident in the 3-D
671 storm structure, where 'AOW' more accurately represents wind profiles across the entire atmosphere, including at low altitudes,
672 where the actual risks to offshore wind energy infrastructure occur. The enhanced performance of the fully coupled model is
673 primarily attributed to ocean wave-induced mixing, which leads to further cooling of the SST. Additionally, the reduced surface
674 roughness length and lower drag coefficient associated with atmosphere-ocean-wave interactions in 'AOW' simulation help
675 maintain a more realistic dynamical representation of the storm structure. In contrast, excessive friction and surface roughness
676 length driven by simplified parameterization (i.e., Charnock relation), in 'AO' simulation, result in increased frictional
677 dissipation of AAM as surface winds strengthen. This additional frictional dissipation, caused by the unrealistically driven
678 surface roughness length over the ocean, weakens tangential wind acceleration, thereby limiting the intensification of the storm
679 during its peak (from 06 UTC to 12 UTC on 22nd August 2021). As a result, 'AO' shows weaker storm wind speeds despite
680 having a more intense minimum SLP compared to 'AOW' during this period. This suggests that incorporating wave dynamics
681 in 'AOW' plays an important role in accurately simulating TC behaviour, ultimately enhancing predictive capabilities for storm
682 intensity and structure.

683
684 Additionally, the fully coupled 'AOW' experiment is characterized by weaker surface enthalpy, leading to a more stable
685 atmospheric boundary layer, reduced surface roughness, and lower TKE, all resulting from an improved representation of
686 dynamic and thermodynamic processes through coupled interactions. This leads to a more realistic simulation of wind veer,
687 with values closer to observations compared to the other two simulations. This finding indicates that, depending on location,
688 the coupling of ocean and waves can significantly affect wind veer, which is not considered in the current IEC standard
689 (Sanchez Gomez et al. 2023). Moreover, the model effectively captures wind-wave misalignment in comparison to buoy
690 observations. This misalignment poses a critical risk to offshore infrastructure, which atmospheric-only and atmosphere-ocean
691 coupled models are unable to predict.

692
693 Although we used Category 1 Hurricane Henri to validate the newly developed fully coupled model (C-WFS) and to highlight
694 the impact of coupling processes on the intensity, structure, and evolution of TCs, the same framework has also been tested
695 for higher-category hurricanes, including Laura (2020), a Category 4 storm that underwent rapid intensification. The results
696 reveal similar trends, with ocean waves contributing to a decrease in hurricane intensity. However, consistent with prior
697 research (e.g., Yamaguchi et al., 2017; Zhao et al., 2022), the atmospheric-only model tends to underestimate the intensity of



698 high-category TCs, particularly for those with minimum SLP near or below 940 hPa. As a result, the fully coupled model
699 further underestimates the intensity of these high-category storms due to additional wave-induced ocean mixing and
700 subsequent cold wakes. Some previous studies (e.g., Zhao et al., 2017, 2022; Zweers et al., 2015) suggested a promising
701 remedy for this issue, such as incorporating sea spray parameterization. For instance, Zhao et al. (2017, 2022) successfully
702 reproduced the intensities of Typhoons Megi (2010) and Haiyan (2013), both Category 5 equivalent super typhoons, using a
703 fully coupled model that incorporated sea spray parameterization. They demonstrated that sea spray increases the enthalpy
704 flux at the atmosphere-ocean interface, leading to a warmer boundary layer and a more unstable surface layer, which, in turn,
705 provide positive feedback for TC intensification. On the other hand, a recent study (Barr and Chen, 2024) examined the role
706 of sea spray in TC dynamics, showing that its effects are dependent on the storm's intensity. For weaker TCs, such as Category
707 1 storms, sea spray tends to inhibit intensification due to evaporative cooling in the boundary layer, acting as negative feedback.
708 However, as a TC strengthens (e.g., Category 2 or higher), increased spray production begins to contribute positively by
709 warming the boundary layer and enhancing deep convection near the eyewall. This transition highlights spray's dual role:
710 initially opposing intensification in weaker storms but eventually supporting rapid intensification in stronger ones, particularly
711 major hurricanes. While this study is highly informative and pioneering in demonstrating spray's dual role, its hypothesis is
712 based on only four TCs, limiting the generalizability of its conclusions. The precise impact of sea spray on TC structure and
713 intensity remains an open question, warranting further research across a broader range of TC events. In this study, sea spray
714 parameterization is not included in the C-WFS modelling system. However, as part of our ongoing research, we are integrating
715 sea spray into the system to investigate its impact on TC behaviour across various storm intensities. Advancing this work
716 represents a crucial step toward improving TC simulations and deepening our understanding of the associated enhancements.

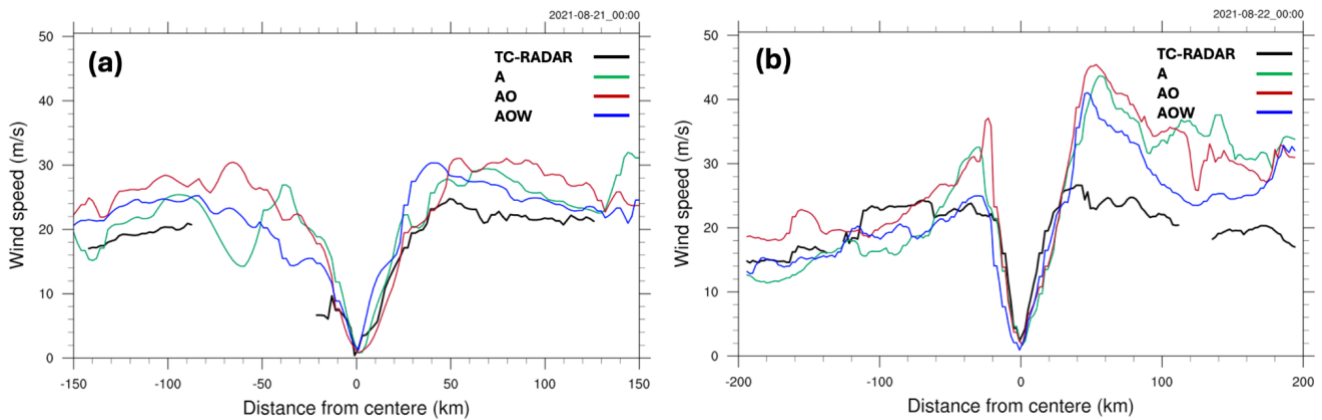
717
718 Another aspect that remains unclear is the impact of the horizontal resolution of the ocean components on TC development
719 within the atmosphere-ocean coupled modelling framework. While the sensitivity of the atmospheric model's resolution to TC
720 representation is well-established, with general consensus suggesting that reducing horizontal grid spacing improves the
721 accuracy of storm intensity predictions (e.g., Gentry and Lakmann, 2010; Taraphdar et al., 2014; Prein et al., 2015), less is
722 understood about how the resolution of ocean components influences TC development. Higher ocean resolution allows for a
723 more detailed representation of mesoscale and submesoscale features (e.g., eddies and fronts affecting SST patterns, Zhang et
724 al., 2023) and their associated atmosphere-ocean interactions, such as heat fluxes, momentum transfer, and upper-ocean mixing
725 processes. These features likely play a critical role in modulating storm-induced SST cooling, redistributing ocean heat content,
726 and influencing the energy supply to TCs. As previously discussed, C-WFS employs an unstructured mesh grid, enabling
727 seamless transitions between coarse and fine resolutions. This approach removes the need for nested grids, commonly used in
728 existing fully coupled models (e.g., COAWST), which can introduce boundary artifacts. Consequently, C-WFS is uniquely
729 equipped to investigate how varying horizontal ocean resolutions affect coupling dynamics and storm development—an area
730 that will be thoroughly explored in future studies.

731



732 **Code and data availability.** The WRF model (Version 4.5.1) is described by Skamarock et al. (2019), and its code is publicly
733 available from <https://github.com/wrf-model/WRF> (University Corporation for Atmospheric Research, 2019). The code for
734 FVCOM (Version 4.3.1., Chen et al., 2003, 2013) for ocean circulation model is publicly available at
735 <https://github.com/FVCOM-GitHub/fvcom>. The SWAN (Version 41.01, Booij et al., 1999) is a third-generation spectral wave
736 model developed at Delft University of Technology that computes random, short-crested wind-generated waves in coastal
737 regions and inland waters (<http://swanmodel.sourceforge.net/>). HYbrid Coordinate Ocean Model (HYCOM; Cummings and
738 Smedstad, 2014) analysis data used for ocean model forcing is available at <http://hycom.org/dataserver/>. NCEP provides
739 Global Forecast System (GFS; NCEP, 2015) data, which is used as atmospheric forcing data, available at
740 <https://www.nco.ncep.noaa.gov/pmb/products/gfs/>. The OSTIA (Good et al., 2020) global sea surface temperature provides
741 daily maps of foundation sea surface temperature at $0.05^\circ \times 0.05^\circ$ available from
742 https://data.marine.copernicus.eu/product/SST_GLO_SST_L4_REP_OBSERVATIONS_010_011/description. The NCL and
743 Python codes for performing analysis and visualization are available at <https://www.ncl.ucar.edu/> and
744 <https://www.python.org/downloads/>, respectively. All simulation data are available from the authors upon request.
745
746

Appendix A: Radial profile of wind speed from the airborne Doppler radar and the three model simulations



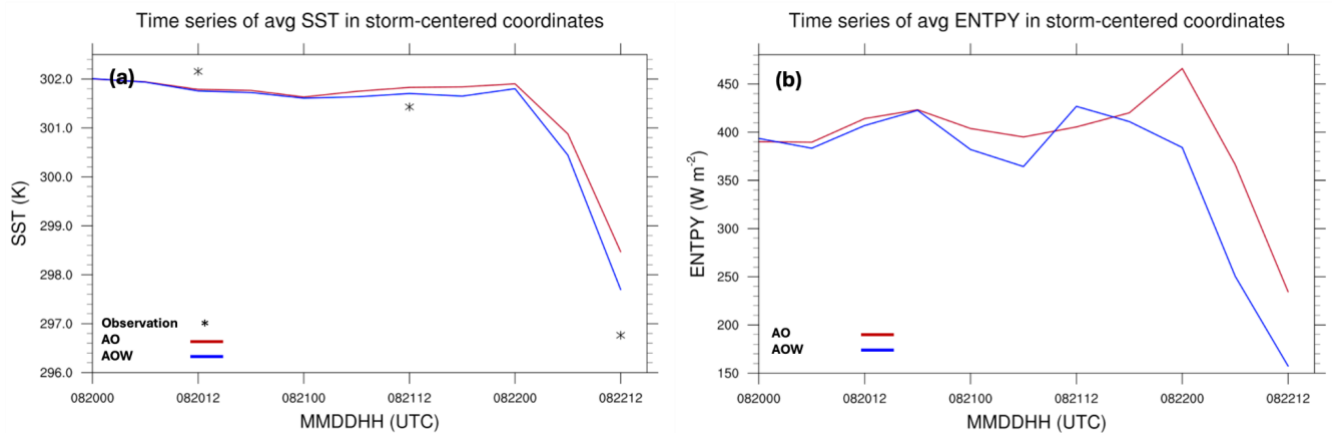
747
748 **Figure A1.** Radial profiles of wind speed from the airborne Doppler radar and the three model simulations are shown in Figure 7
749 for (a) 00 UTC on 21st and (b) 22nd August 2021. The profiles are presented at the 1-km level along the line from A to B, as indicated
750 in Figure 4.

751 752 **Appendix B: Averaged SST and surface enthalpy flux for ‘AO’ and ‘AOW’ in storm-centred coordinate**

753 Figure B1 displays the time series of spatially- averaged SST and surface enthalpy flux in a 300 km x 300 km storm-centred
754 coordinate. Both the time series reveal differences between the two coupled simulations, indicating that ‘AOW’ is associated
755 with cooler SSTs that are closer to the observation, as well as lower surface enthalpy flux over the entire simulation period.
756 This greater cooling of SSTs observed in ‘AOW’ partly explains the reduction in intensity. SST is reduced by the storm through
757 wave-induced vertical mixing and vertical mixed layer depth bringing cold water upward, which in turn reduces TC
758 intensification. Wang et al. (2024b) discussed wave-induced mixing primarily caused by wave breaking and non-breaking
759 wave orbital motion (non-breaking wave). Through their comprehensive literature review, they suggested that wave breaking-
760 induced mixing typically has a limited impact on SST and heat fluxes near the surface, and thus on TC intensity. In contrast,

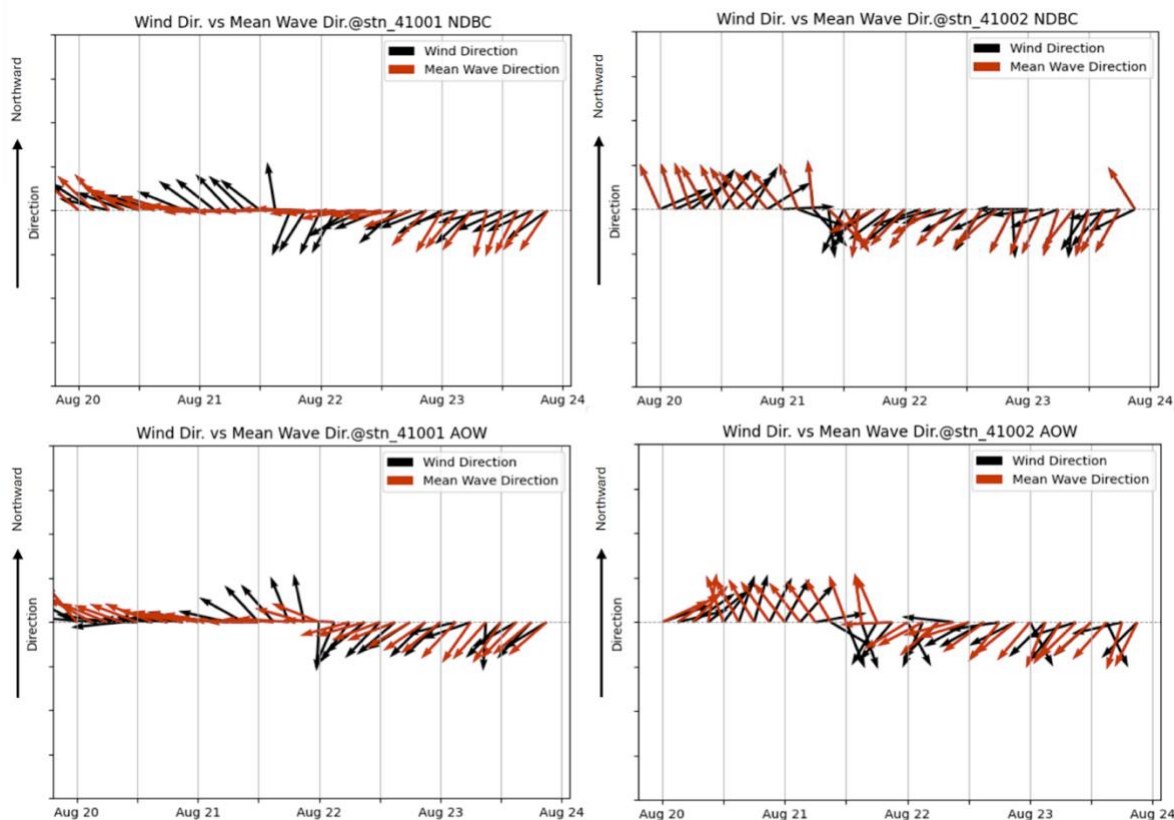


761 non-breaking wave-induced mixing penetrates much deeper, enhancing vertical mixing and mixed-layer depth, which
762 ultimately contributes to a greater reduction in TC intensification. Given this discussion, the inclusion of the non-breaking
763 wave feature in ‘AOW’ may play an important role in moderating the thermal structure of the upper ocean, influencing the
764 exchange of heat and moisture fluxes between the ocean and the atmosphere, and ultimately improving the intensity and
765 structure of Henri.
766



767
768 **Figure B1. Time series of spatial averaged (a) SST and (b) surface enthalpy flux in a 300 km × 300 km storm-centered coordinate.**
769 **Data is derived from OSTIA observation (asterisks), experiment ‘AO’ (red lines), and experiments ‘AOW’ (blue lines).**

770
771 **Appendix C: Simulated and observed surface wind direction and mean ocean wave direction**



772
773 **Figure C1.** Time series comparison of surface wind direction and mean ocean surface wave direction at two NDBC buoy stations,
774 41001 (left column) and 41002 (right column), derived from NDBC buoys (top panel) and experiment ‘AOW’ (bottom panel).

775 **Author contribution.** Conceptualization, Formal analysis, Validation, Visualization: CJ, JW, PX, CH, WP; Data curation,
776 Investigation, Software: CJ, JW, CH, MB, GN; Funding acquisition, Resources, Supervision: JW, PX, WP; Methodology: CJ,
777 CH, WP; Project administration: JW, PX; Writing – original draft: CJ, JW, PX, WP; Writing – review & editing: CJ, JW, PX,
778 CH, MB, GN.

779 **Competing interests.** The authors declare that they have no competing interests.

780 **Acknowledgements.** This study is supported by the Wind Energy Technologies Office (WETO) of the U.S. Department of
781 Energy (DOE) Office of Energy Efficiency and Renewable Energy. The WRF model was made available by the National
782 Center for Atmospheric Research, which is sponsored by NSF. High-Performance Computing support from the Theta cluster
783 operated by Argonne Leadership Computing Facility (ALCF) and Kestrel operated by National Renewable Energy Laboratory
784 (NREL).

785 References

786 Aijaz, S., Ghantous, M., Babanin, A. V., Ginis, I., Thomas, B., and Wake, G.: Nonbreaking wave-induced mixing in upper
787 ocean during tropical cyclones using coupled hurricane-ocean-wave modeling, *J. Geophys. Res.* 122(5), 3939–3963,
788 2017.



- 789 Akinsanola, A. A., Jung, C., Wang, J., & Kotamarthi, V. R.: Evaluation of precipitation across the contiguous United States,
790 Alaska, and Puerto Rico in multi-decadal convection-permitting simulations, *Scientific Reports*, 14(1), 1238, 2024.
- 791 Arthur, W. C.: A statistical–parametric model of tropical cyclones for hazard assessment, *Nat. Hazards Earth Syst. Sci.*, 21,
792 893–916, <https://doi.org/10.5194/nhess-21-893-2021>, 2021.
- 793 Babanin, A. V.: On a wave-induced turbulence and a wave-mixed upper ocean layer, *Geophys. Res. Lett.* 33(20), 1–6,
794 <https://doi.org/10.1029/2006GL027308>, 2006.
- 795 Bardal, L. M., Saetran, L. R., and Wangsness, E.: Performance test of a 3MW wind turbine – Effects of shear and turbulence,
796 *Energy Procedia*, 80, 83–91. <https://doi.org/10.1016/j.egypro.2015.11.410>, 2015.
- 797 Bender, M. A., Ginis I., and Kurihara Y.: Numerical simulations of tropical cyclone–ocean interaction with a high-resolution
798 coupled model, *J. Geophys. Res.*, 98 , 23245–23263, 1993.
- 799 Booij, N., Ris, R. C., and Holthuijsen, L. H.: A third-generation wave model for coastal regions. Part I: Model description
800 and validation, *J. Geophys. Res.*, 104, 7649–7666, doi:10.1029/98JC02622, 1999.
- 801 Cavaleri, L., Fox-Kemper, B., and Hemer, M.: Wind waves in the coupled climate system, *Bull. Amer. Meteor. Soc.*, 93,
802 1651–1661, <https://doi.org/10.1175/BAMS-D-11-00170.1>, 2012.
- 803 Chen, C., Liu, H., and Beardsley, R. C.: An unstructured grid, finite-volume, three-dimensional, primitive equations ocean
804 model: Application to coastal ocean and estuaries, *J. Atmos. Oceanic Technol.*, 20, 159–186,
805 [https://doi.org/10.1175/1520-0426\(2003\)020<0159:AUGFVT>2.0.CO;2](https://doi.org/10.1175/1520-0426(2003)020<0159:AUGFVT>2.0.CO;2), 2003.
- 806 Chen, C., Beardsley, R. C., and Cowles, G.: An unstructured grid, finite-volume coastal ocean model: FVCOM user manual,
807 Tech. Rep. SMAST/UMASSD-13-0701, 416 pp, 2013.
- 808 Chen, F., and Dudhia, J.: Coupling an advanced land-surface/ hydrology model with the Penn State/ NCAR MM5 modeling
809 system. Part I: Model description and implementation, *Mon. Wea. Rev.*, 129, 569–585, 2001.
- 810 Chen, P., Zhang, Z., Li, Y., Ye, R., Li, R., and Song, Z.: The two-parameter Holland Pressure Model for tropical cyclones,
811 *J. Mar. Sci. Eng.* 2024, 12(1), 92; <https://doi.org/10.3390/jmse12010092>, 2024.
- 812 Chen, S. S., Price, J. F., Zhao, W., Donelan, M. A., and Walsh, E. J.: The CBLAST-hurricane program and the next-
813 generation fully coupled atmosphere–wave–ocean models for hurricane research and prediction, *Bull. Am. Meteorol. Soc.*
814 88(3), 311–318, 2007.
- 815 Chen, S. S., Zhao, W., Donelan, M. A., and Tolman, H. L.: Directional wind–wave coupling in fully coupled atmosphere–
816 wave–ocean models: Results from CBLAST-Hurricane, *J. Atmos. Sci.* 70(10), 3198–3215, 2013.
- 817 Churchfield, M. J., and Srinivas, S.: On the effects of wind turbine wake skew caused by wind veer, In 2018 wind energy
818 symposium. American Institute of Aeronautics and Astronautics. <https://doi.org/10.2514/6.2018-0755>, 2018.
- 819 Cione, J. J., and Uhlhorn, E. W.: Sea surface temperature variability in hurricanes: Implications with respect to intensity
820 change, *Mon. Wea. Rev.*, 131, 1783–1796, 2003.
- 821 Craig, P. D. and Banner, M. L.: Modeling wave-enhanced turbulence in the ocean surface layer, *J. Phys. Oceanogr.* 24(12),
822 2546–2559, 1994.
- 823 Craig, A., Valcke, S., and Coquart, L.: Development and performance of a new version of the OASIS coupler, OASIS3-
824 MCT_3.0, *Geosci. Model Dev.*, 10, 3297–3308, <https://doi.org/10.5194/gmd-10-3297-2017>, 2017.



- 825 Cummings, J. A. and Smedstad, O.M.: Ocean data impacts in global HYCOM, *J. Atmos. Ocean. Technol.*, 31 (8), pp. 1771-
826 1791, 10.1175/JTECH-D-14-00011.1, 2014.
- 827 DeMaria, M., Knaff, J. A., and Sampson, C.: Evaluation of long-term trends in tropical cyclone intensity forecasts, *Meteor.*
828 *Atmos. Phys.*, 97, 19–28, 2007.
- 829 DeMaria, M., Sampson, C. R., Knaff, J. A., & Musgrave, K. D.: Is tropical cyclone intensity guidance improving? *Bulletin*
830 *of the American Meteorological Society*, 95(3), 387–398. <https://doi.org/10.1175/bams-d-12-00240.1>, 2014.
- 831 Drennan, W. M.; Graber, H. C.; Hauser, D.; Quentin, C. On the wave age dependence of wind stress over pure wind seas, *J.*
832 *Geophys. Res. Oceans*, 108, 8062, 2003.
- 833 Dyer, A. J., and Hicks, B. B.: Flux-gradient relationships in the constant flux layer, *Quart. J. Roy. Meteor. Soc.*, 96, 715–
834 721, 1970.
- 835 Emanuel, K. A.: An air-sea interaction model of the tropical cyclones. Part I: Steady-State Maintenance, *Journal of the*
836 *Atmospheric Sciences*, 43(6), 585–605. [https://doi.org/10.1175/1520-0469\(1986\)043<0585:AASITF>2.0.CO;2](https://doi.org/10.1175/1520-0469(1986)043<0585:AASITF>2.0.CO;2), 1986.
- 837 Englberger, A., and Lundquist, J. K.: How does wind veer affect the veer of a wind-turbine wake? *Journal of Physics:*
838 *Conference Series*, 1452 (2020) 012068, doi:10.1088/1742-6596/1452/1/012068, 2020.
- 839 Fan, Y., Ginis, I., and Hara, T.: The effect of wind–wave–current interaction on air–sea momentum fluxes and ocean
840 response in tropical cyclones, *J. Phys. Oceanogr.*, 39, 1019–1034, 2009.
- 841 Fan, Y., Ginis, I., and Hara, T.: Momentum flux budget across air–sea interface under uniform and tropical cyclone winds,
842 *J. Phys. Oceanogr.*, 40, 2221–2242, 2010.
- 843 Fischer, M. S., Reasor, P. D., Rogers, R. F., and Gamache, J. F.: An analysis of tropical cyclone vortex and convective
844 characteristics in relation to storm intensity using a novel airborne doppler radar database, *Monthly Weather Review*, 150
845 (9), 2255 – 2278, <https://doi.org/https://doi.org/10.1175/MWR-D-21-0223.1>, 2022
- 846 Gao, L., Li, B., and Hong, J.: Effect of wind veer on wind turbine power generation, *Physics of Fluids*, 33(1), 015101.
847 <https://doi.org/10.1063/5.0033826>, 2021.
- 848 Gentry, M. S., and Lackmann, G. M.: Sensitivity of simulated tropical cyclone structure and intensity to horizontal
849 resolution, *Mon. Wea. Rev.*, 138, 688–704, 2010.
- 850 Ghantous, M., and Babanin, A. V.: One-dimensional modeling of upper ocean mixing by turbulence due to wave orbital
851 motion, *Nonlinear Proc. Geophys.*, 21(1), 325–338, doi:10.5194/npg-21-325-2014, 2014a.
- 852 Ghantous, M., and Babanin, A. V.: Ocean mixing by wave orbital motion. *Acta Physica Slovaca*, 64(1), 1–57,
853 doi:10.2478/apsrt-2014-0001, 2014b.
- 854 Good, S., Fiedler, E., Mao, C., Martin, M. J., Maycock, A., Reid, R., Roberts-Jones, J., Searle, T., Waters, J., While, J., and
855 Worsfold, M.: The current configuration of the OSTIA system for operational production of foundation sea surface
856 temperature and ice concentration analyses, *Remote Sens.* 12, 720, doi:10.3390/rs12040720, 2020.
- 857 Hong, S.-Y. and Lim, J.-O.: The WRF single-moment 6-class microphysics scheme (WSM6), *J. Korean Meteor. Soc.*, 42,
858 129–151, 2006.
- 859 Hong, S.-Y., Noh, Y., and Dudhia, J.: A new vertical diffusion package with an explicit treatment of entrainment processes,
860 *Mon. Wea. Rev.*, 134, 2318–2341, 2006.



- 861 Iacono, M. J., Delamere, J. S., Mlawer, E. J., Shephard, M. W., Clough, S. A., and Collins, W. D.: Radiative forcing by
862 long-lived greenhouse gases: Calculations with the AER radiative transfer models, *J. Geophys. Res.*, 113, D13103, 2008.
- 863 IEC: Wind turbines - part 1: Design requirements (No. IEC 61400-1:2019), 2019a.
- 864 IEC: Wind turbines – part 3: Design requirements for offshore wind turbines (No. IEC 61400-3-1:2019), 2019b
- 865 Itiki, R., Manjrekar, M., Di Santo, S. G., Itiki, C.: Method for spatiotemporal wind power generation profile under hurricanes:
866 US-Caribbean super grid proposition, *Renew. Sust. Energ. Rev.*, 173, Article 113082, 2023.
- 867 Jimenez, P., Dudhia, J., Gonzalez-Ruoco, J. F., Navarro, J., Montavez, J. P., and Garcia-Bustamente, E.: A revised scheme
868 for the WRF surface layer formulation, *Mon. Wea.Rev.*, 140, 898–918, 2012.
- 869 Kapoor, A., Ouakka, S., Arwade, S. R., Lundquist, J. K., Lackner, M. A., Myers, A. T., Worsnop, R. P., and Bryan, G. H.:
870 Hurricane eyewall winds and structural response of wind turbines, *Wind Energy Sci.*, 5, 89–104,
871 <https://doi.org/10.5194/wes-5-89-2020>, 2020.
- 872 Knapp, K. R., Kruk, M. C., Levinson, D. H., Diamond, H. J., and Neumann, C. J.: The international best track archive for
873 climate stewardship (ibtracs) unifying tropical cyclone data. *Bulletin of the American Meteorological Society*, 91 (3),
874 363–376, 2010.
- 875 Knutson, T. and Coauthors: Tropical cyclones and climate change, *Nature Geoscience*, 3(3), 157-163.
876 <https://doi.org/10.1038/ngeo779>, 2010.
- 877 Knutson, T., and Coauthors: Tropical cyclones and climate change assessment: Part I: Detection and attribution, *Bull Amer.*
878 *Meteor. Soc.*, 100, 1987–2007, <https://doi.org/10.1175/BAMS-D-18-0189.1>, 2019.
- 879 Knutson, T., and Coauthors: Tropical cyclones and climate change assessment: Part II: Projected response to anthropogenic
880 warming, *Bull. Amer. Meteor. Soc.*, 101, E303–E322, <https://doi.org/10.1175/BAMS-D-18-0194.1>, 2020
- 881 Komen, G. J., Hasselmann K., and Hasselmann K.: On the existence of a fully developed wind-sea spectrum, *J. Phys.*
882 *Oceanogr.*, 14, 1271–1285, doi:10.1175/1520-0485(1984)014<1271:OTEOAF>2.0.CO;2, 1984.
- 883 Kouadio, K., Bastin, S., Konare, A., and Ajayi, V. O.: Does convection-permitting simulate better rainfall distribution and
884 extreme over Guinean coast and surroundings? *Climate Dynamics*, 55, 153–174. [https://doi.org/10.1007/s00382-018-](https://doi.org/10.1007/s00382-018-4308-y)
885 [4308-y](https://doi.org/10.1007/s00382-018-4308-y), 2020.
- 886 Lane, E. M., Restrepo, J. M., and McWilliams, J. C.: Wave–current interaction: A comparison of radiation–stress and vortex-
887 force, *J. Phys. Oceanogr.* 37, 1122–1141, 2007.
- 888 Li, X., Pu, Z., and Gao, Z.: Effects of roll vortices on the evolution of hurricane harvey during landfall, *J. Atmos. Sci.*, 76,
889 1847–1867, <https://doi.org/10.1175/JAS-D-20-0270.1>, 2021.
- 890 Liu, J., Curry, J. A., Clayson, C. A., and Bourassa, M. A.: High-resolution satellite surface latent heat fluxes in North Atlantic
891 hurricanes, *Mon. Wea. Rev.*, 139, 2735–2747, 2011.
- 892 Madsen, O. S., Poon, Y. K., and Graber, H. C.: Spectral wave attenuation by bottom friction: Theory, *Proceedings of the*
893 *International Conference on Coastal Engineering*, No. 21, 492-506, 1988.
- 894 Mellor, G.: On theories dealing with the interaction of surface waves and ocean circulation, *J. Geophys. Res.* 121(7), 4474–
895 4486, <https://doi.org/10.1002/2016JC011768>, 2016.
- 896 Mogensen, K. S., Magnusson, L., and Bidlot, J.-R.: Tropical cyclone sensitivity to ocean coupling in the ECMWF coupled
897 model, *J. Geophys. Res. Oceans*, 122, 4392–4412, <https://doi.org/10.1002/2017JC012753>, 2017.



- 898 Montgomery, M. T., and Smith, R. K.: Paradigms for tropical cyclone intensification, *Australian Meteorological and*
899 *Oceanographic Journal*, 64, 37–66. <https://doi.org/10.22499/2.6401.005>, 2014.
- 900 Müller, S., Larsén, X. G., and Verelst, D. R.: Tropical cyclone low-level wind speed, shear, and veer: sensitivity to the
901 boundary layer parameterization in the Weather Research and Forecasting model, *Wind Energ. Sci.*, 9, 1153–1171,
902 <https://doi.org/10.5194/wes-9-1153-2024>, , 2024.
- 903 Murphy, P., Lundquist, J. K., and Fleming, P.: How wind speed shear and directional veer affect the power production of a
904 megawatt-scale operational wind turbine, *Wind Energ. Sci.*, 5, 1169–1190, 2020 [https://doi.org/10.5194/wes-5-1169-](https://doi.org/10.5194/wes-5-1169-2020)
905 2020, 2020.
- 906 Nakanishi, M. and Niino, H.: Development of an improved turbulence closure model for the atmospheric boundary layer, *J.*
907 *Meteor. Soc. Japan*, 87, 895–912, doi:<http://dx.doi.org/10.2151/jmsj.87.895>, 2009.
- 908 National Data Buoy Center (NDBC), NOAA: National Data Buoy Center (NDBC) Moored Buoy and C-MAN Station Data,
909 UCAR/NCAR - Earth Observing Laboratory, DOI: <https://doi.org/10.26023/V640-H29S-MR0S>, 2008.
- 910 National Centers for Environmental Prediction (NCEP), National Weather Service, NOAA: U.S. Department of Commerce,
911 Research Data Archive at the National Center for Atmospheric Research, Computational and Information Systems
912 Laboratory, <https://doi.org/10.5065/D65D8PWK>, 2015.
- 913 Olabarrieta, M., Medina, R., and Castanedo, S.: Effects of wave-current interaction on the current profile, *Coastal Eng.*
914 57(7), 643–655, 2010.
- 915 Olson, J. B., Kenyon, J. S., Angevine, W. M., Brown, J. M., Pagowski, M., and Sušelj, K.: A description of the MYNN-
916 EDMF scheme and coupling to other components in WRF-ARW, NOAA Tech. Memo. OAR GSD, 61, 37 pp.,
917 <https://doi.org/10.25923/n9wm-be49>, 2019.
- 918 Paulson, C. A.: The mathematical representation of wind speed and temperature profiles in the unstable atmospheric surface
919 layer, *J. Appl. Meteor.*, 9, 857–861, 1970.
- 920 Perrie, W., Ren, X., Zhang, W., and Long, Z.: Simulation of extratropical Hurricane Gustav using a coupled atmosphere-
921 ocean-sea spray model, *Geophys. Res. Lett.* 31(3), L03110, <https://doi.org/10.1029/2003GL018571>, 2004.
- 922 Perrie, W., Andreas, E. L., Zhang, W., Li, W., Gyakum, J., and McTaggart-Cowan, R.: Sea spray impacts on intensifying
923 midlatitude cyclones, *J. Atmos. Sci.* 62(6), 1867–1883, 2005.
- 924 Prakash, K. R., Pant, V., and Nigam, T.: Effects of the sea surface roughness and sea spray-induced flux parameterization
925 on the simulations of a tropical cyclone, *J. Geophys. Res.* 124(24), 14037–14058, <https://doi.org/10.1029/2018JD029760>,
926 2019.
- 927 Pringle, W. J. and Kotamarthi, V. R.: Coupled ocean wave-atmosphere models for offshore wind energy. Argonne, IL.
928 <https://doi.org/10.2172/1829093>, 2021.
- 929 Qiao, F., Yuan, Y., Yang, Y., Zheng, Q., Xia, C., and Ma, J.: Wave-induced mixing in the upper ocean: Distribution and
930 application to a global ocean circulation model, *Geophys. Res. Lett.* 31(11), L11303,
931 <https://doi.org/10.1029/2004GL019824>, 2004.
- 932 Qing, Y. and Wang, S.: Multi-decadal convection-permitting climate projections for China’s Greater Bay Area and
933 surroundings, *Clim Dyn.* <https://doi.org/10.1007/s00382-021-05716-w>, 2021.



- 934 Rappaport, E. N., and Coauthors: Advances and challenges at the National Hurricane Center, *Wea. Forecasting*, 24, 395–
935 419, 2009.
- 936 Richter, D. H. and Stern, D. P.: Evidence of spray-mediated air-sea enthalpy flux within tropical cyclones, *Geophys. Res.*
937 *Let.* 41(8), 2997–3003, <https://doi.org/10.1002/2014GL059746>, 2014.
- 938 Robertson, A. N., Shaler, K., Sethuraman, L., and Jonkman, J.: Sensitivity analysis of the effect of wind characteristics and
939 turbine properties on wind turbine loads, *Wind Energy Science*, 4(3), 479–513. <https://doi.org/10.5194/wes-4-479-2019>,
940 2019.
- 941 Roldán M., Montoya R. D., Rios J. D., Osorio A. F.: Modified parametric hurricane wind model to improve the asymmetry
942 in the region of maximum winds, *Ocean Eng.* 280, 114508. doi: 10.1016/j.oceaneng.2023.114508, 2023.
- 943 Sanchez Gomez, M., and Lundquist, J. K.: The Effects of Wind Veer During the Morning and Evening Transitions, *Journal*
944 *of Physics: Conference Series*, 1452 (2020) 012075, doi:10.1088/1742-6596/1452/1/012075, 2020.
- 945 Sanchez Gomez, M., Lundquist, J. K., Mirocha, J. D., and Arthur, R. S.: Investigating the physical mechanisms that modify
946 wind plant blockage in stable boundary layers, *Wind Energ. Sci.*, 8, 1049–1069, <https://doi.org/10.5194/wes-8-1049-2023>,
947 2023.
- 948 Schade, L. R., and Emanuel K. A.: The ocean's effect on the intensity of tropical cyclones: Results from a simple coupled
949 atmosphere–ocean model, *J. Atmos. Sci.*, 56 , 642–651, 1999.
- 950 Skamarock, W.C., Klemp, J.B., Dudhia, J., Gill, D.O., Liu, Z., Berner, J., Wang, W., Powers, J.G., Duda, M.G., and Barker,
951 D.M.: A description of the advanced research WRF model version 4; National Center for Atmospheric Research: Boulder,
952 CO, USA, 2019; p. 145, 2019.
- 953 Smagorinsky, J.: General circulation experiments with the primitive equations, part I: the basic experiment *Monthly Weather*
954 *Review*, 91 (1963), pp. 99-164, 1963.
- 955 Smith, J. A.: Wave–current interactions in finite depth, *J. Phys. Oceanogr.* 36(7), 1403–1419, 2006.
- 956 Smith, R. K., Montgomery, M. T., and Van Sang, N.: Tropical cyclone spin-up revisited. *Quarterly Journal of the Royal*
957 *Meteorological Society*, 135(642), 1321–1335. <https://doi.org/10.1002/qj.428>, 2009.
- 958 Smith, A. B.: 2010–2019: A landmark decade of U.S. billion-dollar weather and climate disasters. NOAA,
959 [https://www.climate.gov/news-features/blogs/beyond-data/2010-2019-landmark-decade-us-billion-dollar-weather-and-](https://www.climate.gov/news-features/blogs/beyond-data/2010-2019-landmark-decade-us-billion-dollar-weather-and-climate)
960 [climate](https://www.climate.gov/news-features/blogs/beyond-data/2010-2019-landmark-decade-us-billion-dollar-weather-and-climate), 2020.
- 961 Stull, R. B.: *An Introduction to Boundary Layer Meteorology*, Kluwer, Dordrecht, [https://doi.org/10.1007/978-94-009-](https://doi.org/10.1007/978-94-009-3027-8)
962 [3027-8](https://doi.org/10.1007/978-94-009-3027-8), 1988.
- 963 Sullivan, P. P. and McWilliams, J. C.: Dynamics of winds and currents coupled to surface waves, *Annu. Rev. Fluid Mech.*
964 42(1), 19–42, 2010.
- 965 Sun, X., Xue, M., Brotzge, J., McPherson, R. A., Hu, X.-M., and Yang, X.-Q.: An evaluation of dynamical downscaling of
966 Central Plains summer precipitation using a WRF-based regional climate model at a convection-permitting 4 km
967 resolution, *Journal of Geophysical Research: Atmosphere*, 121, 13801–13825. <https://doi.org/10.1002/2016JD024796>,
968 2016.
- 969 Taylor, P. K., and Yelland, M. J.: The dependence of sea surface roughness on the height and steepness of the waves, *J.*
970 *Phys. Oceanogr.*, 31 , 572–590, 2001.



- 971 Tsartsali, E. E., Haarsma, R. J., Athanasiadis, P. J., Bellucci, A., de Vries, H., Drijfhout, S., de Vries, I. E., Putrahasan, D.,
972 Roberts, M. J., Sanchez Gomez, E., and Roberts, C. D.: Impact of resolution on the atmosphere–ocean coupling along the
973 Gulf Stream in global high resolution models, *Clim. Dyn.* 58(11–12), 3317–3333, 2022.
- 974 Wada, A. and Usui, N.: Impacts of oceanic preexisting conditions on predictions of Typhoon Hai-Tang in 2005, *Adv.*
975 *Meteorol.* 2010, 756071, 2010.
- 976 Walsh, K. J. E., and Coauthors: Hurricanes and climate: The U.S. CLIVAR working group on hurricanes, *Bull. Amer.*
977 *Meteor. Soc.*, 96(6), 997–1017, <https://doi.org/10.1175/BAMS-D-13-00242.1>, 2015.
- 978 Walsh, K. J. E., and Coauthors: Tropical cyclones and climate change, *WIREs Climate Change*, 7, 65–89,
979 <https://doi.org/10.1002/wcc.371>, 2016.
- 980 Wang, J., Deskos, G., Pringle, W. J., Haupt, S. E., Feng, S., Berg, L. K., Churchfield, M., Biswas, M., Musial, W., Muradyan,
981 P., Hendricks, E., Kotamarthi, R., Xue, P., Rozoff, C. M., and Bryan, G.: Impact of tropical and extratropical cyclones on
982 future U.S. offshore wind energy. *Bulletin of the American Meteorological Society*, 1506–1513.
983 <https://doi.org/10.1175/bams-d-24-0080.1>, 2024a.
- 984 Wang, J., Hendricks, E., Rozoff, C. M., Churchfield, M., Zhu, L., Feng, S., Pringle, W. J., Biswas, M., Haupt, S. E., Deskos,
985 G., Jung, C., Xue, P., Berg, L. K., Bryan, G., Kosovic, B., and Kotamarthi, R.: Modeling and observations of North
986 Atlantic cyclones: Implications for U.S. Offshore wind energy. *Journal of Renewable and Sustainable Energy*,
987 16(052702). <https://doi.org/10.1063/5.0214806>, 2024b.
- 988 Warner J. C., Armstrong, B., He, R., Zambon, J. B.: Development of a coupled ocean–atmosphere–wave–sediment transport
989 (COAWST) modeling system. *Ocean Model* 35:230–244. doi:10.1016/j.oceanmod.2010.07.010, 2010.
- 990 Webb, E. K.: Profile relationships: The log-linear range, and extension to strong stability, *Quart. J. Roy. Meteor. Soc.*, 96,
991 67–90, 1970.
- 992 Wei, J., Jiang, GQ., and Liu, X.: Parameterization of typhoon-induced ocean cooling using temperature equation and
993 machine learning algorithms: an example of typhoon Soulik (2013), *Ocean Dynamics* 67, 1179–1193.
994 <https://doi.org/10.1007/s10236-017-1082-z>, 2017.
- 995 Wright, C. W., and Coauthors: Hurricane directional wave spectrum spatial variation in the open ocean, *J. Phys. Oceanogr.*,
996 31, 2472–2488, 2001.
- 997 Wu, L., Rutgersson, A., Sahlée, E., and Guo Larsén, X.: Swell impact on wind stress and atmospheric mixing in a regional
998 coupled atmosphere-wave model, *Journal of Geophysical Research: Oceans*, 121, 4633–4648.
999 <https://doi.org/10.1002/2015JC011576>, 2016.
- 1000 Yablonsky, R. M., and Ginis, I.: Limitation of one-dimensional ocean models for coupled hurricane–ocean model forecasts,
1001 *Mon. Wea. Rev.*, 137, 4410–4419, doi:10.1175/2009MWR2863.1, 2009.
- 1002 Yamaguchi, M., Ishida, J., Sato, H., and Nakagawa, M.: WGNE intercomparison of tropical cyclone forecasts by operational
1003 nwp models: A quarter century and beyond, *Bulletin of the American Meteorological Society*, 98(11), 2337–2349.
1004 <https://doi.org/10.1175/bams-d-16-0133.1>, 2017.
- 1005 Zambon, J. B., He, R., and Warner, J. C.: Investigation of Hurricane Ivan using the coupled ocean–atmosphere–wave–
1006 sediment transport (COAWST) model, *Ocean Dynamics*, 64(11), 1535–1554. [https://doi.org/10.1007/s10236-014-0777-](https://doi.org/10.1007/s10236-014-0777-7)
1007 7, 2014.



- 1008 Zambon, J. B., He, R., Warner, J. C., and Hegermiller, C. A.: Impact of SST and surface waves on Hurricane Florence
1009 (2018): A coupled modeling investigation. *Weather and Forecasting*, 36(5), 1713–1734. [https://doi.org/10.1175/WAF-D-](https://doi.org/10.1175/WAF-D-20-0171.1)
1010 20-0171.1, 2021.
- 1011 Zhang, S., Yuan, Y., and Zheng, Q.: Modeling of the eddy viscosity by breaking waves, *Acta Oceanol. Sin.* 26(6), 116–123,
1012 2007.
- 1013 Zhang, S., Xu, S., Fu, H., Wu, L., Liu, Z., Gao, Y. et al.: Toward earth system modeling with resolved clouds and ocean
1014 submesoscales on heterogeneous many-core HPCs, *Nat. Sci. Rev.* 10(6), nwad069, 2023.
- 1015 Zhao, B., Wang, G., Zhang, J. A., Liu, L., Liu, J., Xu, J., et al.: The effects of ocean surface waves on tropical cyclone
1016 intensity: Numerical simulations using a regional atmosphere-ocean-wave coupled model, *Journal of Geophysical*
1017 *Research: Oceans*, 127, e2022JC019015. <https://doi.org/10.1029/2022JC019015>, 2022.
- 1018 Zhao, B., Qiao, F., Cavaleri, L., Wang, G., Bertotti, L., and Liu, L.: Sensitivity of typhoon modeling to surface waves and
1019 rainfall. *Journal of Geophysical Research: Oceans*, 122(3), 1702–1723. <https://doi.org/10.1002/2016jc012262>, 2017.
- 1020 Zhou, X., Hara, T., Ginis, I., D’Asaro, E., and Reichl, B. G.: Evidence of langmuir mixing effects in the upper ocean layer
1021 during tropical cyclones using observations and a coupled wave-ocean model, *Journal of Geophysical Research*, 2(10),
1022 <https://doi.org/10.1029/2023JC020062>, 2023.
- 1023 Zhu, T., and Zhang, D.-L.: The impact of the storm-induced SST cooling on hurricane intensity, *Adv. Atmos. Sci.*, 23, 14–
1024 22, 2006.
- 1025